STRUCTURE OF TURBULENT CHANNEL FLOW PERTURBED BY CYLINDRICAL ROUGHNESS ELEMENTS

BY

GOKUL PATHIKONDA

THESIS

Submitted in partial fulfillment of the requirements
for the degree of Master of Science in Aerospace Engineering
in the Graduate College of the
University of Illinois at Urbana-Champaign, 2013

Urbana, Illinois

Advisor:

Professor Kenneth T. Christensen

ABSTRACT

The current study investigates the structural modifications imposed in fully-developed turbulent channel flow by an isolated, wall-mounted circular cylinder. The cylinder height is chosen to specifically extend into the logarithmic layer of the flow in order to study its perturbation of the larger flow scales that embody a significant fraction of the turbulent kinetic energy. Hot-wire measurements were made in the wake of the wall-mounted circular cylinder at multiple wall-normal and streamwise positions. Mean streamwise statistics (mean velocity and Reynolds normal stress) and pre-multiplied spectra of perturbed and unperturbed flow were computed, and influence of the cylinder on these statistics were analyzed. The influence of such perturbations on the inner-outer interactions of the channel flow were also investigated.

Besides the mean velocity deficit in the wake of the cylinder, a new peak in streamwise Reynolds normal stress away from the wall was observed, coupled with the suppression of the near-wall peak native to the incoming unperturbed flow. Pre-multiplied spectra elaborated on these energy modifications, specifically the occurrence of an energy peak corresponding to a wavelength (λ_x) ~ 0.45 times the channel half-height (h), an attenuation of large-scale energy close to the wall, and a tertiary peak at two-third's the cylinder height corresponding to a length scale of $\lambda_x \sim 10h$. Further, amplitude modulation effects of the large-scale motions on small scales close to the wall, representative of inner–outer interactions, was found to be greatly enhanced in the near-wall region. All the perturbations were found to decay with streamwise

distance downstream towards the unperturbed flow.

A clear persistence of the structures at the aforementioned tertiary peak, similar to the wavelengths of the very large scale motions (VLSMs) in canonical wall turbulence, tends to suggest an environment in turbulent flows preferring structures of such wavelengths. Possible mechanisms for the observed suppression of near-wall cycle and the enhanced inner–outer interactions are suggested. The influence of cylinder aspect ratio on the characteristics of perturbed flow are evaluated, and a distinction in wake structure is identified. The necessity of future studies to further understand these significant attributes of perturbation response and recovery of the turbulent wall bounded flows is highlighted.

ACKNOWLEDGMENTS

I consider myself fortunate to be working under the able guidance and supervision of Professor Kenneth Christensen, to whose continual motivation and support, I am deeply grateful. His constant feedback, meticulous and intuitive pedagogy, and a friendly environment for discussion have all given me the research acumen that I have developed.

I would also like to gratefully acknowledge all the enthusiastic professional and personal advises that I received from my friends, particularly at LTCF, with which my research turned out to be the pleasurable experience that it did— Sohan Kale, Julio Barros, Gianluca Blois, Taehoon Kim- just to name a few. Their support is gratefully appreciated, and am looking forward for a lot more research in their company.

I would like to thank Professor Ivan Marusic, University of Melbourne, for sharing his valuable experience in computing 1-D spectra. I am highly thankful to the administrative staff at Aerospace Engineering and MechSE, particularly Staci Tankersley and Kathy Smith, for continual support and patient assistance throughout my program. I also would like to thank Gregory Milner of Aerospace Engineering machine shop, who built most of my experimental equipment with remarkable precision.

On a more personal note, I am thoroughly indebted to the continual support and love from my family (my sister and brother-in-law, Pavani and Praveen Rao in particular) without whose selfless support, my career wouldn't have been as easy as it has been.

TABLE OF CONTENTS

1 INTRODUCTION

1.1 Literature Review

Turbulent wall-bounded flows have been found to be populated by a broad range of self-sustaining coherent structures in the inner and outer layers of the flow, the presence of which has explained various dynamic observations. Particle image velocimetry (PIV) measurements in streamwise–wall-normal planes (Adrian et al., 2000; Christensen and Adrian, 2001; Hommema, 2001) show coherent vortex structures, and low momentum regions that are well explained by the hairpin vortex paradigm. The significance of the vortex structures as one of the primary sources of the Reynolds stress generating Q2 (ejection) and Q4 (sweep) events (Ganapathisubramani et al., 2003; Adrian, 2007), their suspected role in creation of the very long streamwise streaks of alternating low and high momentum throughout the log layer (Tomkins, 2001; Tomkins and Adrian, 2003; Balakumar and Adrian, 2007), the robustness of the structures even at very large Reynolds numbers (Hommema, 2001; Adrian, 2007; Hommema and Adrian, 2003), and more recently, the strong footprint of these log layer coherent structures on the streamwise fluctuations of the near-wall cycle (Hutchins and Marusic, 2007; Mathis et al., 2009a,b) only show these structures as one of the important dynamic quantities of turbulent wall-bounded flows. The influence of wall roughness on these co-

herent structures has been of primary interest in many works (Tomkins and Adrian, 2003; Guala et al., 2012). The dynamic importance of these structures gives rise to the obvious question — can these structures be altered or manipulated to modify the turbulent boundary layer (or other wall-bounded flows)? Flow perturbations using both static wall protrusions/roughness elements (Tomkins, 2001; Ryan et al., 2011; Ortiz-Dueñas et al., 2011; Jacobi and McKeon, 2011b)) and dynamic roughness elements (Jacobi and McKeon, 2011a)) have been considered in the literature in this regard.

Since hairpin vortices are found to be predominantly populated in the logarithmic region, the current work aims to understand the influence of a single, wall-mounted cylindrical element of small aspect ratio ($AR = 1.75-2.5$) that extends up to the outer edge of the logarithmic layer of a fully-developed turbulent channel flow. Besides large-scale motions (LSM) of streamwise scales of order δ (where δ is the dominant flow dimension: boundary-layer thickness, pipe radius or channel half height) observed in both internal and external turbulent flows, the flows were also observed to embody very-large-scale motions (VLSM) that are several δ in the streamwise direction (Balakumar and Adrian, 2007; Monty et al., 2009). The structural changes imposed by such a cylindrical element to the turbulent channel flow and its influence on the LSMs, VLSMs and their growth will be investigated in the current work. The current experimental work and analysis are similar to that of Ryan et al. (2011) and Jacobi and McKeon (2011b).

Various studies have been performed to understand the wake structures shed by cylinders in cross flows. In particular, the wake of an infinite cylinder in a uniform cross flow has attracted significant interest owing to a rel-

atively complex flow with an easy experimental setup. While the dynamic characteristics of such flow have been captured both theoretically and experimentally since Kármán's analysis (Williamson, 1996), the flow across finite cylinders, which are of higher practical significance, still waits to be fully understood. A finite length cylinder mounted on a wall with a free end in the flow sheds various kinds of vortices and structures adding to the complexity of measurement and analysis. A number of studies have attempted to understand the flow trailing a finite wall-mounted obstacle, and the effect of the geometric and flow parameters (Adaramola et al., 2006; Sakamoto and Arie, 1983; Leder, 2003; Sumner et al., 2004; Tanaka and Murata, 1999; Pattenden et al., 2005; Wang and Zhou, 2009). While combinations of these possible conditions open up to a wide range of practical scenarios, only the pertinent fraction of the literature concerning the interests of the current work are emphasized upon here. In particular, studies with finite cylinders of small aspect ratios ($AR \sim 2-7$), partially or fully submerged in a boundary layer, and those dealing with the structure of the wake, are discussed.

It can be summarized that there are three significant parameters that influence the vortex shedding of a finite wall-mounted cylinder: the aspect ratio (AR) of the cylinder, the height (H) of the cylinder relative to the incident flow length scale, δ, and the nature of the incident flow (Sakamoto and Arie, 1983). The dominant structures observed to be shed by a finite cylinder in a cross flow for various combinations of above factors can be seen further to be of three kinds: the horseshoe vortex structure at the wall-cylinder junction, the Kármán vortices around the mid-span of the cylinder, and the tip vortices shed by the free end of the cylinder in the flow (Pattenden et al., 2005). Thus, a cellular variation of Strouhal number along the height of

the cylinder is expected, depending on structure(s) dominant at any given location (Farivar, 1981). However, though the aforementioned three kinds of vortices are the well observed structures in high AR cylinders, mutual interaction with each other or with the other structures in the incident flow might lead to one or more of them to be dominant or suppressed. For example, at low AR, the downwash due to vortex shedding from the tip of the cylinder has been found to influence and suppress the formation of the pair of vortices arising the from the base of the cylinder (different from the horseshoe vortex) in its wake (Sumner et al., 2004). A methodological set of experiments, dealing with the influence of the shape and geometry of the cylinder relative to the flow, was performed by Sakamoto and Arie (1983). In this work, the dominant frequency of vortex shedding at cylinder mid height was quantified as a power law (as $St = C(H/d)^n$, where St is the Strouhal number corresponding to the dominant frequency, C and n are constants depending on the incident flow, and H and d are the height and diameter of the cylinder, respectively). A definitive change in the shedding behavior has been observed to occur at a 'critical' aspect ratio ($AR \sim 2.5$ for cylinder) at which the aforementioned power-law constants vary abruptly. This behavior, supported by observations from flow visualizations, has been attributed to the formation of symmetric arch-type vortices, instead of anti-symmetric Kármán type vortices that are observed at higher AR. It was further noted in the same study that for still smaller aspect ratios ($AR < 1.5$), no prominent vortex shedding frequency was observed over the background fluctuations of the flow. Later studies (Okamoto and Sunabashiri, 1992; Tanaka and Murata, 1999) have also indicated the presence of such arch type vortices from wake measurements of low AR cylinders. The formation of arch type vortices with smaller AR cylinders was accounted to the increased strength of

the separated shear layer from the tip of the cylinder and the subsequent interaction with the Kármán vortices from the lateral surfaces (Sumner et al., 2004). Other notable differences in the wake, such as the absence of pairs of vortices at the base of the cylinder (Sumner et al., 2004), absence of a local minimum streamwise velocity at the cylinder mid-height (Adaramola et al., 2006), unicellular variation of Strouhal number along the height (Sakamoto and Arie, 1983; Farivar, 1981), and a broader peak of vortex shedding frequencies (Sakamoto and Arie, 1983), have all been reported in the literature for small AR cylinders in a cross flow.

Besides aspect ratio, efforts to investigate the influence of the nature of incident flow on vortex shedding from a finite cylinder are relatively few. Sakamoto and Arie (1983) observed that, for right-rectangular prisms, the critical aspect ratio (at which the vortex shedding changes from anti-symmetric to symmetric arch type) did not change with the height of the prism relative to incident turbulent boundary layer, at least for the range of obstacle heights considered, i.e. $H/\delta = 0.42$ to 1.40. Further, the AR at which no prominent shedding frequency was observed over the background flow spectrum was found to be constant at $AR \sim 1.5$ for all H/δ values considered. Similarly, Park and Lee (2002) made hot-wire measurements and flow visualization for a finite cylinder and found that the downwash from the separated layer at the tip of the cylinder was stronger (and hence a smaller shedding frequency) with an incident atmospheric boundary layer, than it was with a uniform incident flow. Wang et al. (2006) also have investigated the influence of laminar and turbulent boundary layers incident on a finite cylinder, and found that the turbulent boundary layers strengthen the vortices that originate from the base of the cylinder. It must, however, be noted

that these studies in Wang et al. (2006) are on cylinders that are only partly submerged in the boundary layer of the incident flow, and hence the incident boundary layer is interacting directly only with the base of the cylinder.

While the above studies consider cylinders of heights comparable with the length scales of the incident flow (say, the boundary-layer thickness), the studies investigating cylinders with low H/δ, i.e. cylinders fully submerged within the log layer of a turbulent wall-bounded flow, are investigated more as isolated roughness elements than they are as flows across cylinders. Tomkins (2001) investigated flow across both single and an array of wall mounted cylinders and hemispheres of heights 100 and 200 viscous wall units in a fully turbulent boundary layer. The wake of hemispheres was found to have higher population (than cylinders) of vortices similar to horseshoe heads and the low momentum regions akin to those associated with hairpin packets. Further, no definite shedding periodicity was found with either obstacles considered, possibly due to the small aspect ratio and the influence of upstream turbulence. While there is extensive literature (Guala et al., 2012; Wu and Christensen, 2007) available on the influence of wall roughness perturbing only the inner region of turbulent wall bounded flows (i.e. small relative roughness), such literature is deliberately not elaborated upon here, as such perturbations to the flow can be deemed to be significantly different from the current analysis on log-layer perturbations.

The most pertinent literature to the current work seems to be those of Ryan et al. (2011) and Jacobi and McKeon (2011b). Besides an array of cylinders, the former also analyzes the flow trailing a single cylinder element fully submerged within the log layer of a turbulent boundary layer as in the current

study. Mean velocity and streamwise turbulent intensity variations in the flow trailing the cylinder have been measured. It was further noted that the inner streamwise turbulence intensity peak, that was observed in the clean incident flow, is weakened, and a new second peak appears farther away from the wall. As the flow convects downstream, this second peak continuously diminishes, and the near-wall peak re-appears as the flow relapses to the clean turbulent boundary layer. Similar observations downstream of 2-D wall protrusions (an array of transverse rectangular strips spanning the entire flow) perturbing a turbulent boundary layer were found in Jacobi and McKeon (2011b). The pre-multiplied spectra at various wall-normal and streamwise locations indicated that the disturbance caused by the roughness elements did not affect the entire energy spectrum uniformly, and that selective scales were enhanced or suppressed. Other studies, with arrays of cylinders (Ortiz-Dueñas et al., 2011; George, 2005; Zheng, 2013) and hemispheres (Guala et al., 2012; Tomkins, 2001) as wall roughness elements, have investigated the influence of shed vortices on the overall organization and interaction of vortex packets in the inner and outer regions of turbulent boundary layers.

1.2 Current Work

The current work investigates the influence of a single, wall-normal cylindrical element extending towards the outer boundary of the log-layer in a turbulent channel flow. The investigations, akin to that of Ryan et al. (2011), are made on cylinders of varying aspect ratios and heights relative to the channel half-height, and are made by the single-component constant tem-

perature thermal anemometry (CTA) technique. Only perturbations from a single cylinder to the channel flow are considered for the current study, with emphasis on the streamwise velocity fluctuations and spectra downstream of the cylinder. The influence of the cylinder, and the structures shed on the incident flow are explored using the pre-multiplied spectra of fluctuating flow in the cylinder wake. The discrepancy spectra, which highlights the differences between the incident unperturbed flow structures and the perturbed flow structures, are also computed. Finally, the effect of the cylinder on the 'inner–outer' interactions of incident canonical turbulent channel flow, the possible explanations for the trends, are investigated with the time series measurements made using a hot-wire.

The measurements and analysis in the current study, not only aim to capture the perturbing mechanisms of a single cylinder in the channel flow, but also the subsequent evolution of the same in the streamwise direction. The results are compared with others in the literature Ryan et al. (2011); Jacobi and McKeon (2011b), and similarities and distinctions from these studies are highlighted. Finally, the current work is expected to add to the existing state of knowledge on the perturbation response of turbulent wall-bounded flows.

2 EXPERIMENTS

2.1 Experimental Facility

The current experimental work was conducted in the Laboratory for Turbulence and Complex Flow in a closed circuit channel flow facility with a test section of rectangular cross-section of dimensions $50\,\text{mm} \times 600\,\text{mm}$ (i.e. $25\,\text{mm}$ channel half-height, h). The working fluid is air and flow is driven by a 5 HP cent-axial blower. The air from the blower, after passing through a honey comb, set of screens and a smooth contraction section, was then allowed to develop over a channel length of $6\,\text{m}$ ($\sim 240h$) before the measurements were made. A removable ceiling at the measurement location provided access to the interior of the test section for mounting of probes and cylinders. Seven pairs of wall pressure taps were spaced along the flow development length, starting from $0.7\,\text{m}$ from the P-type sandpaper trip placed immediately downstream of the converging section. Each pair of pressure ports comprised wall taps mounted in the top and bottom walls of the channel (across the 'height'). Gauge pressure measurements were made at the wall pressure ports to measure the pressure gradient in the channel flow using a Validyne DP103-18 pressure transducer and a Validyne CD15 Carrier Demodulator. A least linear fit to the pressure measurements made at these ports gives the pressure gradient in the channel flow, which in turn, can be used to estimate the viscous scales of the turbulent channel flow,

such as wall shear stress ($\tau_w = h\frac{dP}{dx}$, P is the measured pressure), friction velocity ($u_\tau = (\tau_w/\rho)^{1/2}$, ρ is the density of the fluid), viscous length scale ($y^* = \nu/u_\tau$, ν is the kinematic viscosity of the fluid) and the friction Reynolds number ($Re_\tau = h/y^*$). These, along with the other flow parameters of the experiments, are elaborated on in Section 2.3, Table 2.3. A T-Type 'Omega' thermocouple was mounted into the flow near the wall at the trip location to monitor the fluid temperature throughout the experiments.

2.2 Hot-Wire Anemometry

All of the hot-wire measurements reported in this work were made using a Dantec 90C10 CTA module mounted on a Dantec 90N10 frame. A gold plated Dantec 55P05 boundary layer probe, with a 1.25 mm long sensing length on a 5 μm diameter Tungsten wire, was mounted in the flow using a Dantec 55H21 straight probe support. It must be noted that the sensor length (in viscous units, $l^+ \approx 62$) is larger than what is recommended by Hutchins et al. (2009) for resolving the energy content of the smallest scales of the flow. Thus, significant attenuation in the small-scale energy is expected, particularly near the wall where the energy in small scales is relatively the highest (Hutchins et al. (2009)). However, this attenuation does not affect the general conclusions made from the current experiments where the larger scales are of interest. The probe and the probe support were translated using a computer-controlled Velmex UniSlide translation stage, with a minimum step size of 1.6 μm, translating the probe normal to the wall. Dantec Streamware software was used to acquire data, while Matlab was used to control the translation stage, measure temperature and trigger

the hot-wire data acquisition. An 11-megapixel TSI 12-bit scientific grade CCD camera and a 180 mm lens, with four 12 mm PK-12 and one 27.5 mm PK-3 spacers between the camera and the lens, were mounted outside the channel, with the field of view coinciding with the streamwise–wall-normal measurement plane. This gave a magnification of 12μm/pix to accurately monitor the positions of the cylinder from the sensor and the sensor from the wall. The camera was calibrated using a printed dot matrix target at the location of the hot-wire probe. The probe was placed manually near the wall, the hot-wire sensor distance from the wall was measured using the camera, and the measurements were initiated. Matlab would then move the probe to pre-determined wall-normal locations, triggering and waiting for data acquisition at each position. The same trigger to the data acquisition was also fed to the camera system, which would then take an image of the hot-wire probe at each corresponding measurement position.

The hot-wire CTA system was operated at an over-heat ratio of 0.8, which, in a 18 m/s laminar flow, had a frequency response of 40 kHz to a standard square-wave test. In-situ calibration was not suitable for the current work due to absence of a laminar flow region inside the channel, and hence, the calibration was done in an external dedicated calibration facility. The probe could be transferred to and from the experimental setup by disconnecting a single connection, to minimize the changes in the system resistance, if any, due to connections. The entire system was calibrated before and after the experiments using an external calibration nozzle facility at 30 different laminar flow velocities ranging from 2–18 m/s, with pitot static and hot-wire probes in tandem.

Figure 2.1 shows a schematic of the hot-wire calibration nozzle facility. It is driven by an 0.25 HP electric blower that drives air to a settling chamber. A conical bypass valve is used to bleed air out of the system before it enters the settling chamber, effectively controlling the volume (and hence velocity) of the air through the calibration nozzle. The air from the settling chamber is then passed through a honeycomb and a screen to a stagnation chamber. It then passes through a $5:1$ converging section, to the nozzle exit, giving a top-hat laminar velocity profile at the exit. The hot-wire and a pitot-static probe are mounted at the nozzle exit at radially symmetric positions for calibrations. A Validyne DP103-06 pressure transducer, with Validyne CD-23 carrier demodulator was used to measure the pressure difference from the pitot static probe for smaller velocities ($\sim 2 - 7\,\mathrm{m/s}$), and a Validyne DP103-18 pressure transducer with Validyne CD-15 carrier demodulator was used for higher velocities ($\sim 5 - 20\,\mathrm{m/s}$). Calibration velocity at the nozzle exit was controlled by adjusting the conical screw-mounted bypass valve. Temperature measurements of the air using a T-type 'Omega' thermocouple were made in the chamber, simultaneously with pitot-static and hot-wire measurements, and corrections to measured CTA bridge voltage were applied using the relation (Bruun, 1996)

$$E_{\mathrm{ref}} = E_m \left(\frac{T_w - T_{a,\mathrm{ref}}}{T_w - T_a} \right)^{1/2}, \tag{2.1}$$

where E_{ref} is the corrected bridge voltage at the reference air temperature $T_{a,\mathrm{ref}}$, E_m is the measured voltage at air temperature T_a, and T_w is the wire temperature (which remains constant in a CTA system). The total drift in temperature through the duration of the calibration, due to the heating from the blower, did not exceed $1.5\,^{\circ}\mathrm{C}$ in any of the calibrations. Each of the 30

Table 2.1: Hot-Wire parameters and Bridge settings

Parameter	Value
Reference temperature (T_{ref})	24.2 °C
Operating Wire TemperatureT_w	226 °C
Over-heat ratio	0.8
Wire resistance at T_{ref}	4.188 Ω
Decade resistance	183.568 Ω
Signal conditioner offset	2.086 V
Signal conditioner amplifier gain	8
Sampling frequency	70 kHz
Duration of each time series	30 s

calibration points consisted of a 15 second average of pitot-static, hot-wire and thermocouple measurements. A 4^{th} order polynomial regression fit was made on the corrected bridge voltage and the measured velocity points.

Three calibrations were performed before the experimental measurements were initially made. The hot-wire probe was then mounted in the channel facility, and the channel flow measurements (detailed in the following section) were completed sequentially. After all the channel flow measurements, the hot-wire probe was re-mounted on the calibration facility, and one calibration was done again to check for any drift in calibration. The average of the pre- and post-experiment calibrations was used to calculate the velocities from hot wire signal. Figure 2.2 shows all the calibration curves, and Table 2.1 lists the various hot-wire parameters used for the experiments. The maximum discrepancy between velocities from various calibrations was found to be less than 2.5% over the entire range. All the measurements from the channel flow were made at 70 kS/s (35 kHz Nyquist Frequency, $\Delta t^+ \sim 0.5$) for 30 seconds ($\sim 21600 t_h$, t_h being the turnover time, $= h/U_h$), allowing the capture of the smallest and largest significant flow scales (Mathis et al., 2009a).

2.3 Experimental Parameters

For all the experiments reported in the current work, measurements were made at 46 logarithmically spaced wall-normal locations within the first 20 mm from the wall, and 10 linearly spaced locations within the next 10 mm. All of the experiments were performed in the aforementioned experimental facility by setting the pressure gradient in the channel to give an $Re_\tau \approx 1250$ ($Re_h \sim 28,000$). A set of experiments (comprising measurements at various streamwise locations) on each cylinder considered to perturb the flow, was preceded and succeeded by unperturbed channel flow measurements (without any cylinder). This was done to observe any possible changes in calibration and/or incident flow between the experiments. Unperturbed channel measurements were also done at $Re_\tau \sim 935$ to compare the velocities with that predicted by DNS simulations (in Del Alamo et al. (2004), "Series L950"), and they compared to within experimental uncertainty.

Two cylindrical dowel pins were considered in the current work as the perturbing elements. A taller and higher AR cylinder of 5 mm height ($H^+ = 250$, $H/h = 0.2$) and 1.96 mm diameter ($D^+ = 98$, $D/h = 0.078$), henceforth designated 'Cylinder - A', had an aspect ratio of 2.55. A shorter and smaller aspect ratio cylinder of 4.18 mm height ($H^+ = 208$, $H/h = 0.17$) and 2.37 mm diameter ($D^+ = 118$, $D/h = 0.095$), and henceforth designated 'Cylinder - B', had an aspect ratio of 1.76. These cylinder parameters are summarized in Table 2.2. The Reynolds number based on the diameter of the two cylinders and velocity at the tip of the cylinders is $Re_H \sim 1800$ and 2100, respectively. The parameters considered were similar to those in Ryan et al. (2011), with the primary differences being the incident flow (channel flow vs. turbulent boundary layer) and the heights of the cylinder with respect

Table 2.2: Cylinder Parameters

Parameter	Cylinder - A	Cylinder - B
Height, H (mm)	5.0	4.18
Diameter, D (mm)	1.96	2.37
Aspect Ratio (H/D)	2.55	1.76
H/h	0.20	0.17
H^+	250	208
D/h	0.078	0.095
D^+	98	118

Table 2.3: Experiment Details

Cylinder	ID	Re_τ	Re_h	U_h (m/s)	u_τ (m/s)	y^* (μm)	x_c/D
Clean	HC1	1237	28,642	18.00	0.78	20.21	–
	LC1	940	21,145	13.26	0.59	26.58	–
Cylinder A	A1	1250	28,875	18.04	0.78	19.93	4.4
	A2	1246	28,971	18.06	0.78	20.06	6.0
	A3	1250	29,006	18.09	0.78	19.99	9.1
Clean	HC2	1249	28,752	18.02	0.78	20.02	–
	LC2	933	21,204	13.26	0.58	26.79	–
Cylinder B	B1	1247	28,817	18.14	0.78	20.05	4.0
	B2	1254	29,066	18.16	0.78	19.94	6.2
	B3	1258	29,199	18.16	0.78	19.87	8.3
Clean	HC3	1251	28,793	18.14	0.79	19.99	–
	LC3	934	21,097	13.25	0.59	26.77	–

to the log layer. For each cylinder, three streamwise positions downstream of the cylinders in the spanwise mid-plane were considered for the measurements. They were placed approximately $4D$, $6D$ and $8D$ downstream of the cylinder axis, and comfortably downstream of the recirculation zone. The calibrated TSI camera, measuring the wall-normal position, was also used to measure the streamwise position of the hot-wire sensor wire with respect to the cylinder axis (and reported in Table 2.3). The cylinders were mounted on the channel wall using a 2-sided glue tape, perpendicular to the wall to within 1° inclination.

Figure 2.3 shows a sample image taken by the camera, during the experiment. A separate image (*not* Figure 2.3), with the channel wall at the measurement plane clearly marked, was taken for every experiment to determine the position of the wall. From the subsequent images, such as one shown in Figure 2.3, the perpendicular distance of the sensor from the wall was determined, by knowing the magnification of the image. The streamwise distance between the cylinder and the hot-wire sensor was also determined using the same technique.

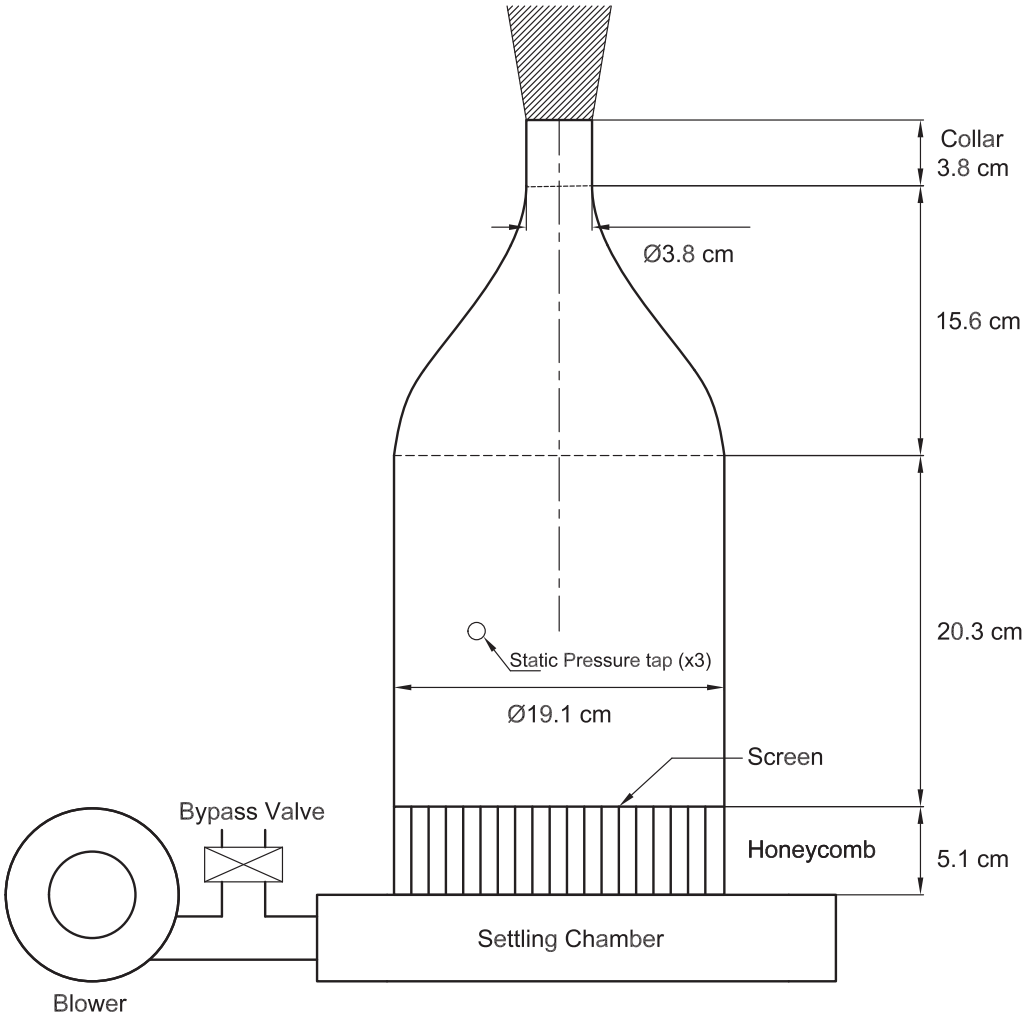

Figure 2.1: A schematic of laminar jet calibration facility used to calibrate the hot-wire system. The hot-wire probe and a pitot-static probe were mounted at the nozzle exit (hatched region). Bypass valve was used to control the velocity of the jet. Full details of the system can be found in Hommema (2001).

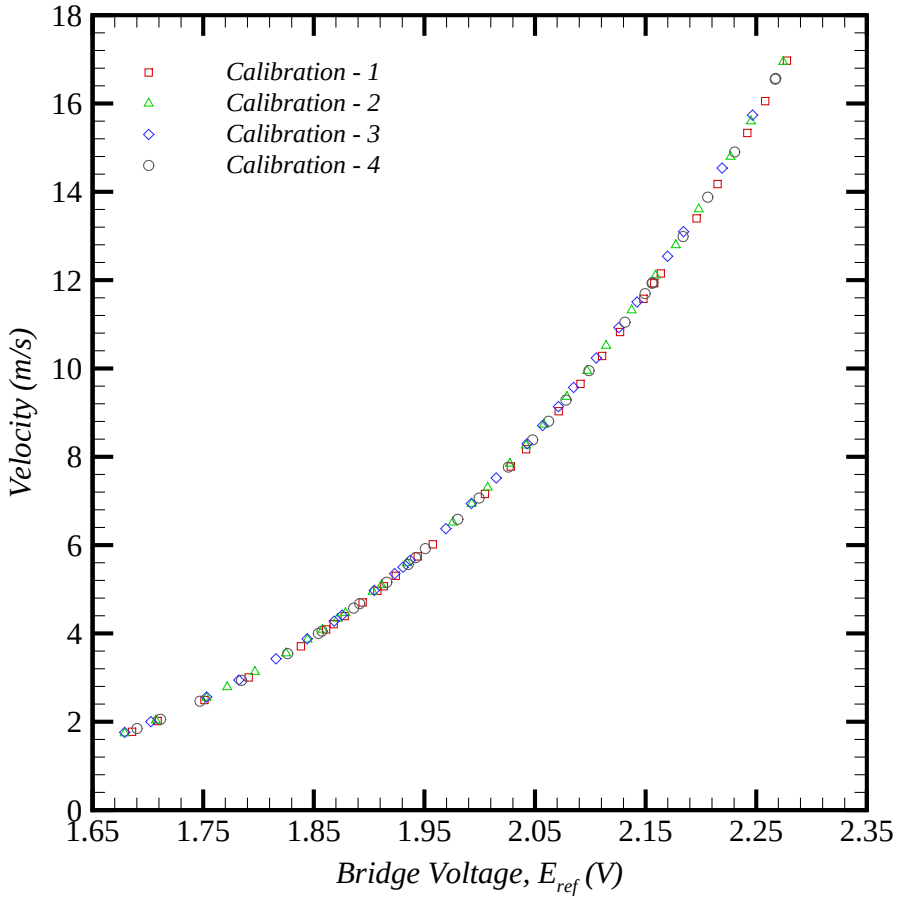

Figure 2.2: Different calibrations performed before and after the experiments. *Calibration - 1,2,3* – before the experiments; *Calibration - 4* – after the experiments.

Figure 2.3: A sample image taken by the TSI position feedback camera used to determine the wall normal position accurately. The image shows the hot-wire probe and the cylinder inside the channel. The flow is from left (cylinder) to right (probe).

3 RESULTS AND ANALYSIS

3.1 Mean Flow Statistics

Mean flow statistics, such as the mean streamwise velocity ($\overline{U}$) and the streamwise Reynolds normal stress ($\overline{u^2}$), were computed for all the experiments listed in Table 2.3. These statistics were computed on a subset of $210,000$ statistically-independent samples from the full time series measurements, to avoid bias. The measurements and comparisons at $Re_\tau \sim 935$ are mentioned here only to test and show the fidelity of the hot-wire measurements, and steadiness of the experimental system, by comparing it with the available DNS data in the literature at this Re_τ. The influence of the cylinder on the flow is analyzed only on $Re_\tau = 1250$, which is consistent with Ryan et al. (2011), and the analysis succeeding this section is only on this latter Re_τ.

Unperturbed Channel Flow

Figure 3.1 shows the mean streamwise velocity of the channel flow measurements at $Re_\tau \sim 935$, alongside the DNS data of Del Alamo et al. (2004). A good agreement between the hot-wire measurements and the DNS predictions can be observed for mean streamwise velocity and the streamwise Reynolds normal stress. The discrepancy in the mean streamwise velocity ($\overline{U}$) between the experiments and the DNS data very close to the wall in Figure 3.1a seems

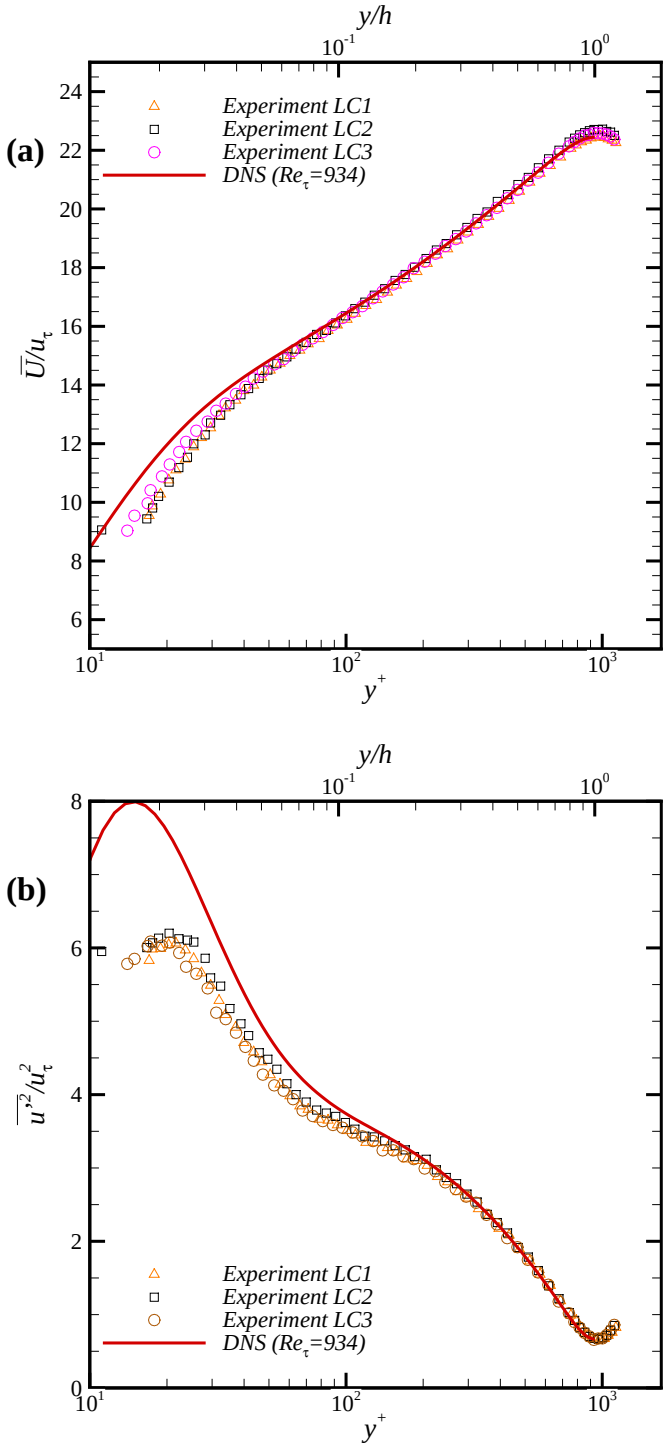

Figure 3.1: *(a)* Mean velocity ($\overline{U}/u_\tau$) and *(b)* streamwise Reynolds normal stress ($\overline{u'^2}/u_\tau^2$) as a function of wall-normal position at $Re_\tau \sim 935$ between various stages of the experiment. Also plotted for comparison are the DNS results of Del Alamo et al. (2004).

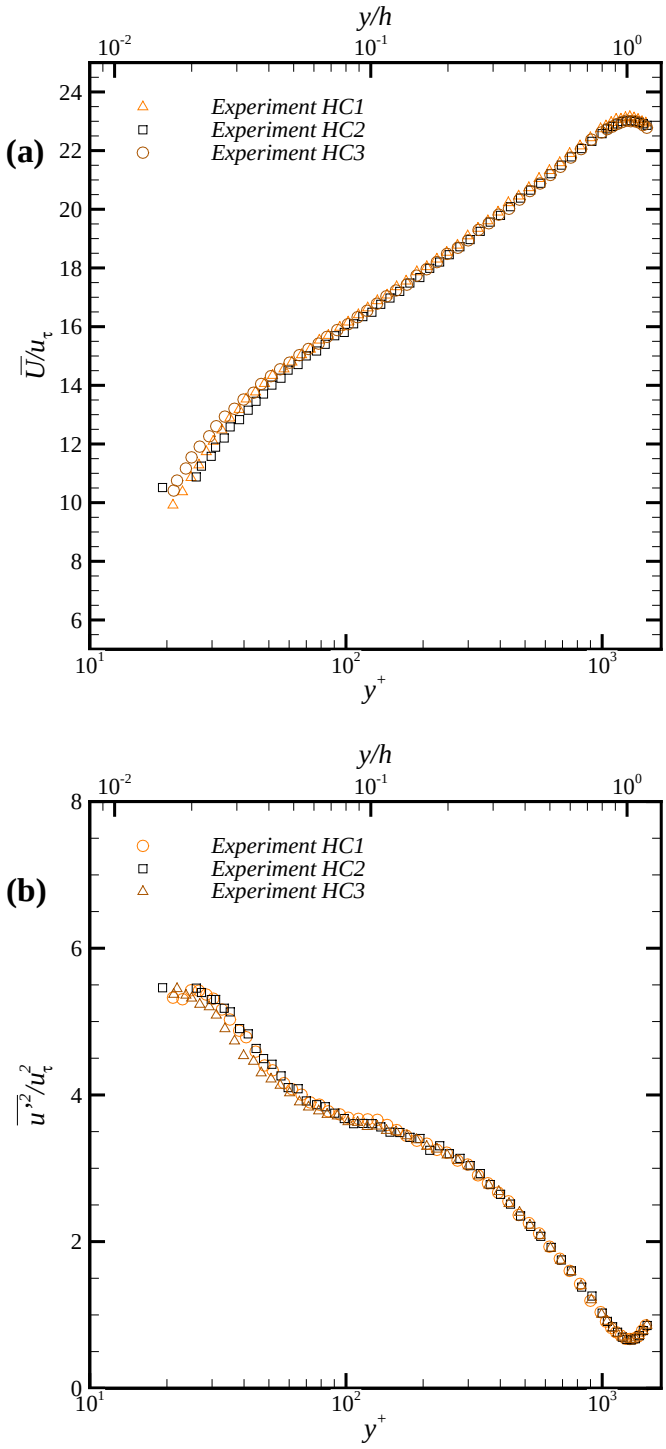

Figure 3.2: *(a)* Mean velocity ($\overline{U}/u_\tau$) and *(b)* streamwise Reynolds normal stress ($\overline{u'^2}/u_\tau^2$) as a function of wall-normal position at $Re_\tau \sim 1250$ between various stages of the experiment.

to arise from uncertainty in determining the wall position. Further, an attenuation of the streamwise Reynolds normal stress ($\overline{u^2}$) very close to the wall can be seen in the hot-wire measurements, when compared with the DNS data. This, as mentioned earlier, can be attributed to the spatial filtering of the small scales by using a larger-than-recommended (Hutchins et al., 2009) hot-wire sensor length. This problem is severe near the wall as seen, where the small-scale energy content is relatively high (Hutchins et al., 2009). Farther from the wall, the significant scales are accurately captured by the hot-wire measurements. Except for this attenuation, the consistency of the results obtained between the three measurements done at various stages of the experiments highlights the stability of the experimental facility and hot-wire system. Similarly, Figure 3.2 shows the mean statistics of the three hot-wire measurements of unperturbed channel flow at $Re_\tau \sim 1250$: HC1, HC2 and HC3 mentioned in Table-2.3. It can be seen that a good good agreement exists between the three measurements, and can thus be concluded that the incident flow on the cylindrical roughness elements and the experimental setup is repeatable.

Perturbed Channel Flow

A similar analysis to that of unperturbed channel flow mentioned in the previous section can be done on the flow perturbed by the cylinder. Figure 3.3a shows the mean velocity and streamwise Reynolds normal stress variation with distance from the wall, at different streamwise positions downstream of the Cylinder - A ($AR = 2.55$). An unperturbed channel flow curve is also shown in the figure for comparison. An obvious velocity deficit in the mean velocity relative to the unperturbed flow can be observed trailing the cylinder, even at the farthest streamwise location measured ($x/D = 9.1$). The

flow, however, seems to be undisturbed from the unperturbed flow, at least in the mean velocity sense, at wall positions above the cylinder tip ($y^+ \geq 250$). It can also be observed that the flow recovery to the unperturbed flow is faster near the wall than it is near the tip of the cylinder, possibly due to the higher velocity gradients at the former location. These trends are similar to those of Ryan et al. (2011), which also shows the mean velocity recovery downstream of a single cylinder.

Besides the mean streamwise velocity, the streamwise Reynolds normal stress ($\overline{u'^2}$) trailing the cylinder can also be compared with the unperturbed flow. Figure 3.3b shows $\overline{u'^2}$ at various y locations measured at different x/D positions downstream of the Cylinder - A. It can be observed that, closest to the cylinder (at $x/D = 4.4$), the near-wall energy peak of the incident flow is suppressed, and a secondary peak previously unobserved in unperturbed channel flow, appears away from the wall at approximately two-thirds of the cylinder height. This secondary peak diminishes in intensity in the subsequent measurements farther downstream, and approaches the unperturbed flow conditions. However, the recovery of the inner peak in $\overline{u'^2}$ of turbulent channel flow has not been detected for Cylinder - A at the first two streamwise locations considered in this study ($x/D = 4.4, 6.1$). Besides these variations in recovery, any perturbation even to this second-order statistic of the incident flow above the cylinder tip ($y^+ > 250$) was not observed. Further details about the distribution among various scales of this increased turbulent kinetic energy is discussed in Section 3.2.

Similar trends can be observed for the smaller aspect ratio Cylinder - B ($AR = 1.76$) wake. Figure 3.4a shows the mean velocity plot. The overall

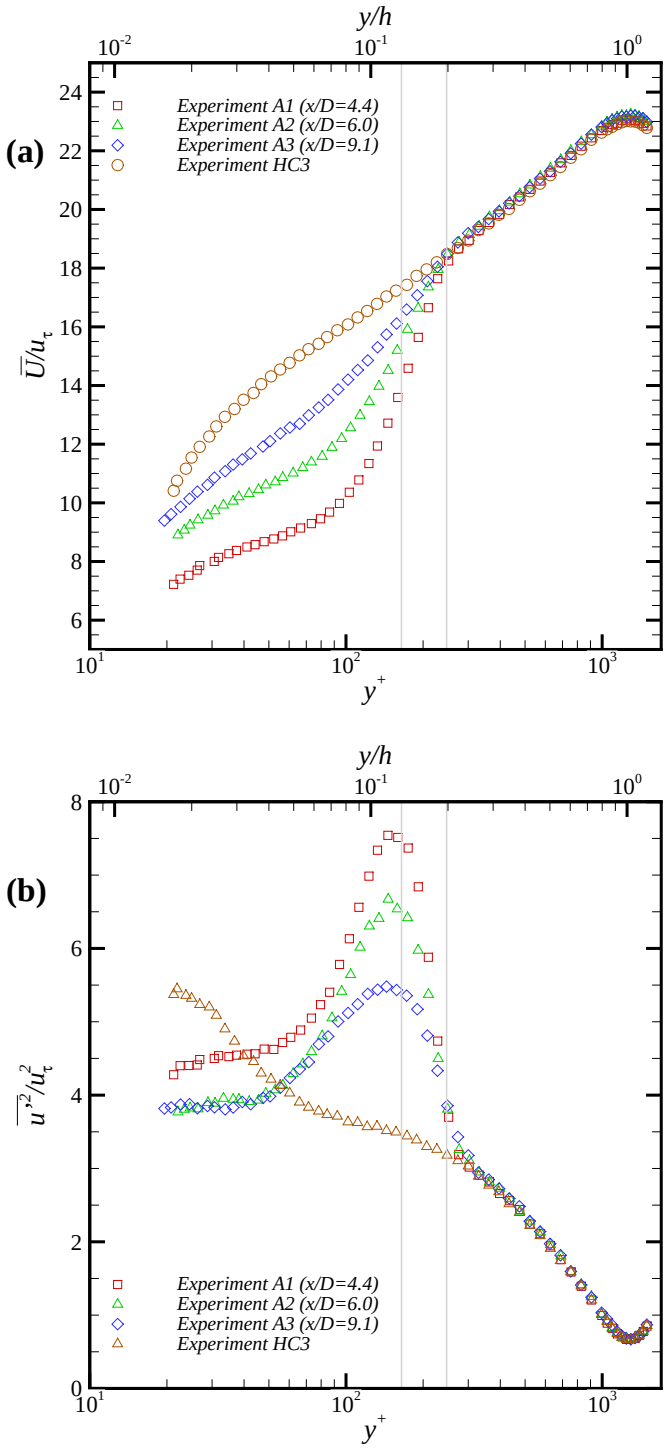

Figure 3.3: *(a)* Mean velocity ($\overline{U}/u_\tau$) and *(b)* streamwise Reynolds normal stress ($\overline{u'^2}/u_\tau^2$) as a function of wall-normal position measured in the wake of the Cylinder-A ($AR = 2.55$) at various streamwise locations. Also plotted are unperturbed incident flow measurements for reference. The two vertical lines indicate the wall-normal locations of the cylinder height and 2/3 of the cylinder height.

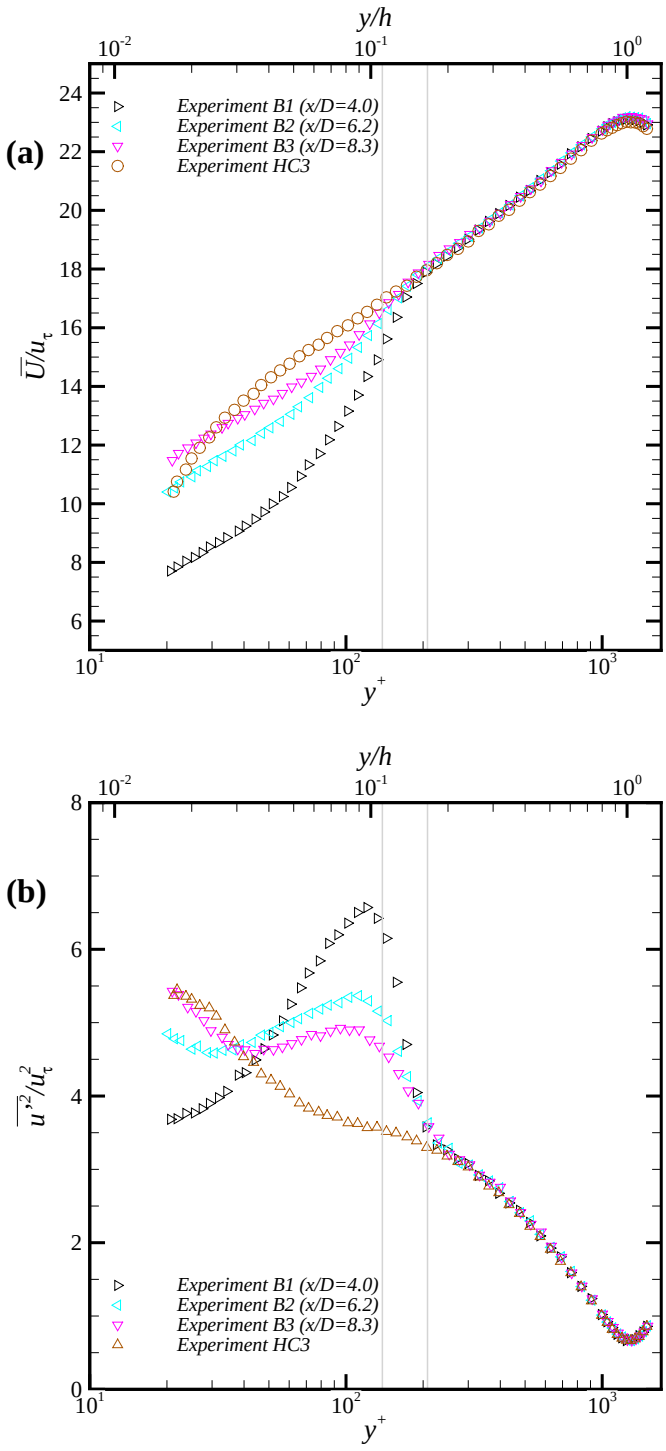

Figure 3.4: As in Figure 3.3 but for Cylinder-B ($AR = 1.76$).

trends of velocity deficit and recovery downstream are similar to Cylinder - A, except close to the wall at the farthest streamwise location ($x/d = 8.3$), where the velocity is observed to be higher than the unperturbed channel flow. Since one would expect an eventual return of the flow to the unperturbed channel flow at a sufficiently large distance downstream, further investigation is required to ascertain this overshoot in the recovery, and the possible reasons. The influence of the aspect ratio can be seen in the velocity profile closer to the wall. While the streamwise velocity profile of the higher aspect ratio Cylinder - A in Figure 3.3 displayed a strong point of inflection close to the wall ($y^+ \sim 40$), the same behavior is much weaker and hardly observable for the Cylinder - B at all the streamwise locations. The overall variation of $\overline{u'^2}$ has many similarities with that of Cylinder-A. The secondary peak, as before, appears at approximately two-thirds of the cylinder height, and is strong closer to the cylinder. This secondary peak progressively diminishes toward the unperturbed flow farther downstream of the cylinder. A simultaneous increase in the inner wall peak, akin to that reported by Ryan et al. (2011), was observed with Cylinder - B, in concert with the diminishing secondary peak. This behavior near the wall was not observed with Cylinder - A (Figure 3.3), where the inner peak recovered only in the farthest streamwise location measured. This recovery, in Cylinder - B, was found to be stronger near the wall than it was at the secondary peak, similar to the mean velocity recovery trend observed earlier for Cylinder A. These differences with aspect ratio in the recovery to the unperturbed flow seem to suggest a different wake structure for the higher aspect ratio cylinder.

It could thus be concluded that the the cylinder perturbs the mean flow such that there is a mean streamwise velocity defect close to the wall, below

the cylinder height. In the streamwise Reynolds normal stress, the perturbed flow shows a new peak of higher turbulent kinetic energy at approximately two-thirds of the cylinder height, and a simultaneous suppression of the near wall peak. The perturbed flow, as it convects downstream of the cylinder, recovers towards the unperturbed channel flow in both cylinder cases. The differences in the near wall recovery between the two cylinders suggest a qualitatively different wake structure, and its dependence on the aspect ratio of the perturbing cylindrical element.

3.2 Pre-Multiplied Spectra

The high sampling rate of the experiments, coupled with the extended length of the time series, enables calculation of the energy distribution as a function of scale. The pre-multiplied auto-spectrum, or simply pre-multiplied spectrum ($k_x\phi_{uu}$), depicts the turbulent kinetic energy among the logarithmically distributed fluctuating scales [$\log(k_x)$], and thus gives a better perception of the energy distribution in the log-log space. It is the product of the wavenumber (k_x) and the auto-spectral density function (ϕ_{uu}). Pre-multiplied spectra reveal the energy distribution among various scales in the streamwise Reynolds normal stress component shown, for example, in Figure 3.2b for unperturbed channel flow at $Re_\tau \sim 1250$. All of the auto-spectra of the current work were computed using the 30 second time-series signal from the hot wire at each y location, which can be assumed into 1-D spatial distribution using the Taylor's frozen field hypothesis using the local mean velocity as the convection velocity. The velocity signal was normalized with the inner scales, averaged using the Welch method with a 50% overlap, and then smoothened

by averaging $6floor(k_x h)^{0.5}$ points on either side of a given wave number k_x (Balasubramaniam, 2002; Bendat and Piersol, 2000). The utility of the smoothening function can be seen in Figure 3.5. A Hanning window was used on signal segments of length 4096 samples, and the energy difference due to windowing was calculated and compensated for appropriately. The frequency domain signal was transformed into the wavenumber domain using the Taylor's frozen-field hypothesis with the local mean velocity at the respective y positions used for the convection velocity of the fluctuating field for all scales. Recent studies (Del Álamo and Jiménez, 2009) have shown the dependence of convective velocities on the scale size. While this would only change the shape of the spectra (by inhomogeneous scaling of the k_x axes), conclusions made in this work on the differences between the unperturbed and perturbed flows will still hold in a relative sense, particularly due to the consistency in the convection velocities used for all cases. A small kink in the spectra was observed at all the measurements at around 3 kHz, irrespective of the flow conditions, as can be seen in Figure 3.5 at $k_x y^* = 0.05$. This, however, was found to be from the CTA module used for these experiments, as also noted in Balakumar and Adrian (2007) and Balasubramaniam (2002) who utilized the same physical CTA. This aberration was extremely local, distinctly identifiable in all the plots, and far from the scales of interest in this effort. It therefore has not influenced in any way the conclusions drawn in this work.

Unperturbed Channel Flow

The pre-multiplied spectrum shown in Figure 3.6 shows the energy distribution as a function of scale at $Re_\tau \sim 1250$ for unperturbed channel flow. The contour plot is the average of the three unperturbed flow measurements

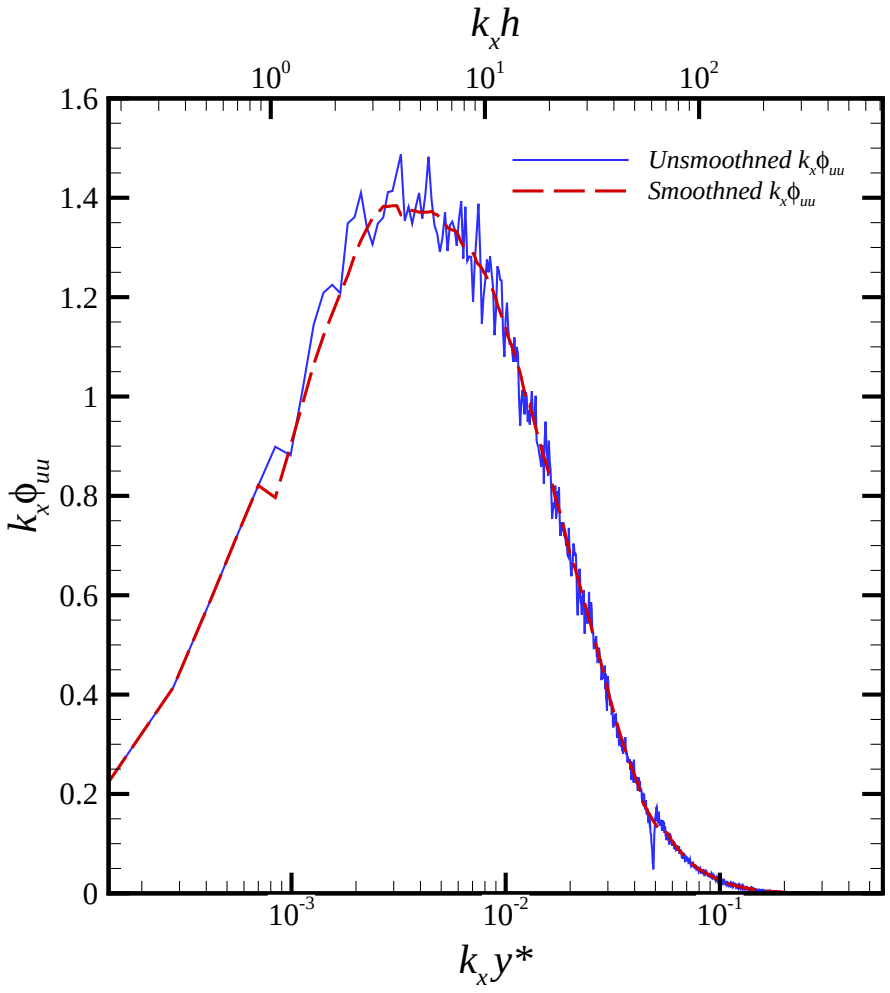

Figure 3.5: A representative actual and smoothened pre-multiplied energy spectra for unperturbed turbulent channel flow.

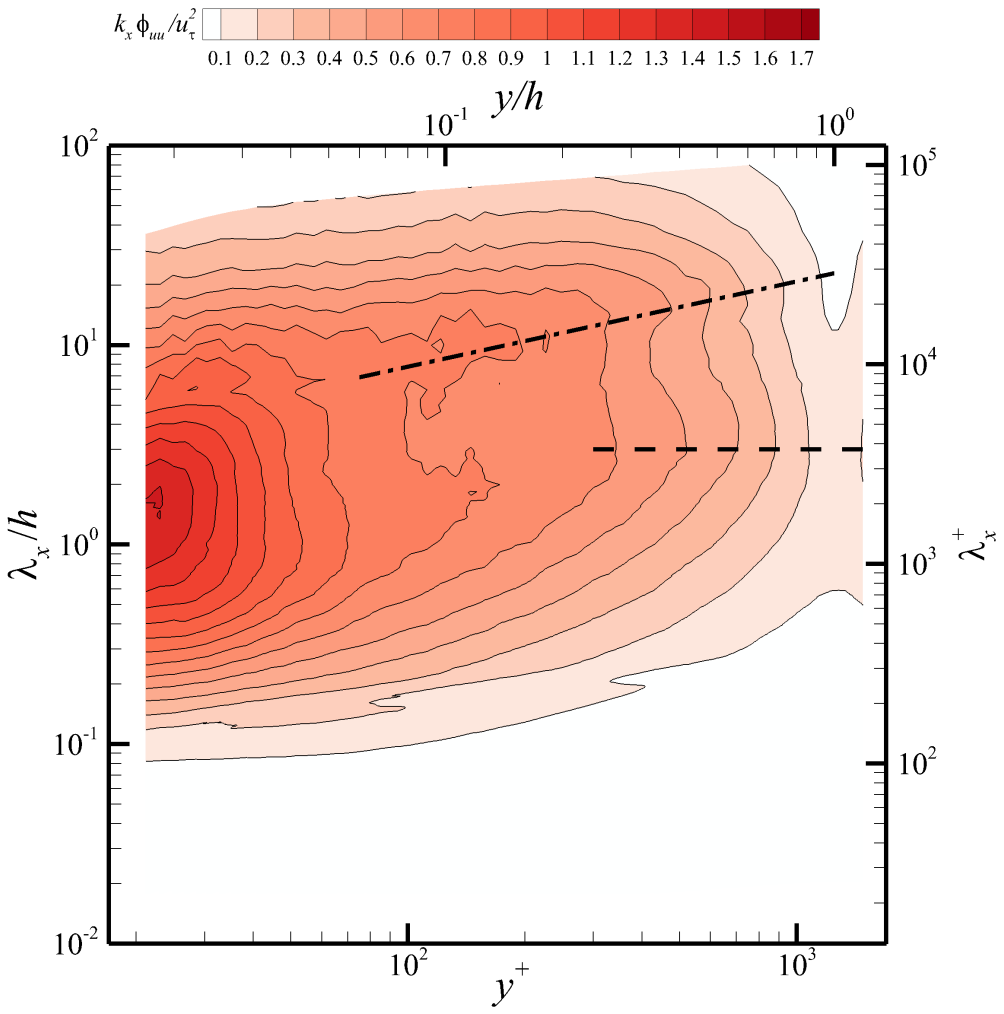

Figure 3.6: Contours of the pre-multiplied energy spectrum ($k_x\phi_{uu}$) for unperturbed incident channel flow, calculated as the average of three measurements (HC1, HC2 and HC3 in Table 2.3). The *dashed-dot* line indicates the predicted VLSM growth observed by Monty et al. (2009) according to Eq. (3.1). The *dashed* line highlights the expected LSM peak at $\lambda_x/h = 3$.

(HC1, HC2, HC3). The results are similar to the observations reported in Ng et al. (2011), showing several key features. The inner near-wall peak can be observed at $\lambda^+ \sim 2000$, which is slightly higher than the inner peak (~ 1000) of canonical turbulent wall-bounded flows. This is likely due to the aforementioned attenuation in the measurement of the small scales owing to the current hot-wire characteristics (i.e., relatively long sensor length). Nevertheless, the energy peak due to the large-scale motions (LSMs) can be observed in the $\lambda/h \sim 3$ region (marked by *dashed* line in the plot) as has been previously reported in the literature (Balakumar and Adrian (2007); Ng et al. (2011)). While there is no clear outer VLSM peak noted in the logarithmic layer in the current relatively low Re_τ measurements, as was observed by Ng et al. (2011) at higher Re_τ, imprints of the VLSMs ($\lambda \sim 10h$) can be observed. This is particularly notable starting from within the logarithmic region, and growing in scale away from the wall. The growth was observed to follow a power law of the form

$$\frac{\lambda_x}{h} = 23 \left(\frac{y}{h}\right)^{\frac{3}{7}}, \tag{3.1}$$

as reported by Monty et al. (2009) and marked by a *dashed-dot* line in Figure 3.6, starting from $y/h = 0.06$ and extending till $y/h = 1$. From these observations, it can be concluded that the incident unperturbed flow in the channel-flow facility embodies all relevant scales, particularly LSMs and VLSMs as previously reported in the literature.

Perturbed Channel Flow

Figure 3.7 (a,c,e) show the pre-multiplied spectra in the wake of Cylinder-A ($AR = 2.55$) at the three streamwise positions where the measurements

were made. As mentioned earlier, the pre-multiplied spectrum gives the distribution of turbulent kinetic energy as a function of scale at a given y^+ location, the integral of which, among all wave numbers, gives the streamwise Reynolds normal stress profiles shown in Figure 3.3. An energy peak at $y^+ \sim 160$ ($y/H \sim 0.64$) of wavelength $\lambda^+ = 562$ ($\lambda/h = 0.45$; $\lambda/D = 5.73$), is observed at all streamwise locations in the perturbed flow. This feature was previously not present in the unperturbed channel flow shown in Figure 3.6. Further, the clear near-wall peak observed in the unperturbed flow at $\lambda^+ \sim 2000$ in Figure 3.6 is simultaneously weakened. The identical distribution of the energy as a function of scale closer to the wall in the wake of Cylinder-A, particularly in the nearest two streamwise locations, complements the observed flattening of the streamwise turbulence intensity seen earlier in Figure 3.3b.

A clearer view of the influence of the cylinder on the incident channel flow can be seen from the perturbation contour maps in Figure 3.7 (b,d,f) that give the difference between the perturbed and the unperturbed flow. First, a significant energy peak at $y^+ \sim 160$ is noted in these discrepancy spectra. This peak is responsible for the increase in the streamwise turbulent energy contributions seen earlier in Figure 3.3. Second, besides this excess energy peak, the discrepancy maps close to the wall also show an addition of smaller-scale energy and a suppression of larger-scale energy (where the discrepancy is negative). This behavior can be rationalized as one of two physical mechanisms: (1) a possible complete substitution of the near-wall cycle by the cylinder wake, or (2) addition of energy at the smaller scales and simultaneous suppression of large-scale energy within the incident turbulent flow due to the cylinder. A closer observation of the large scales ($\lambda/h > 3$) in

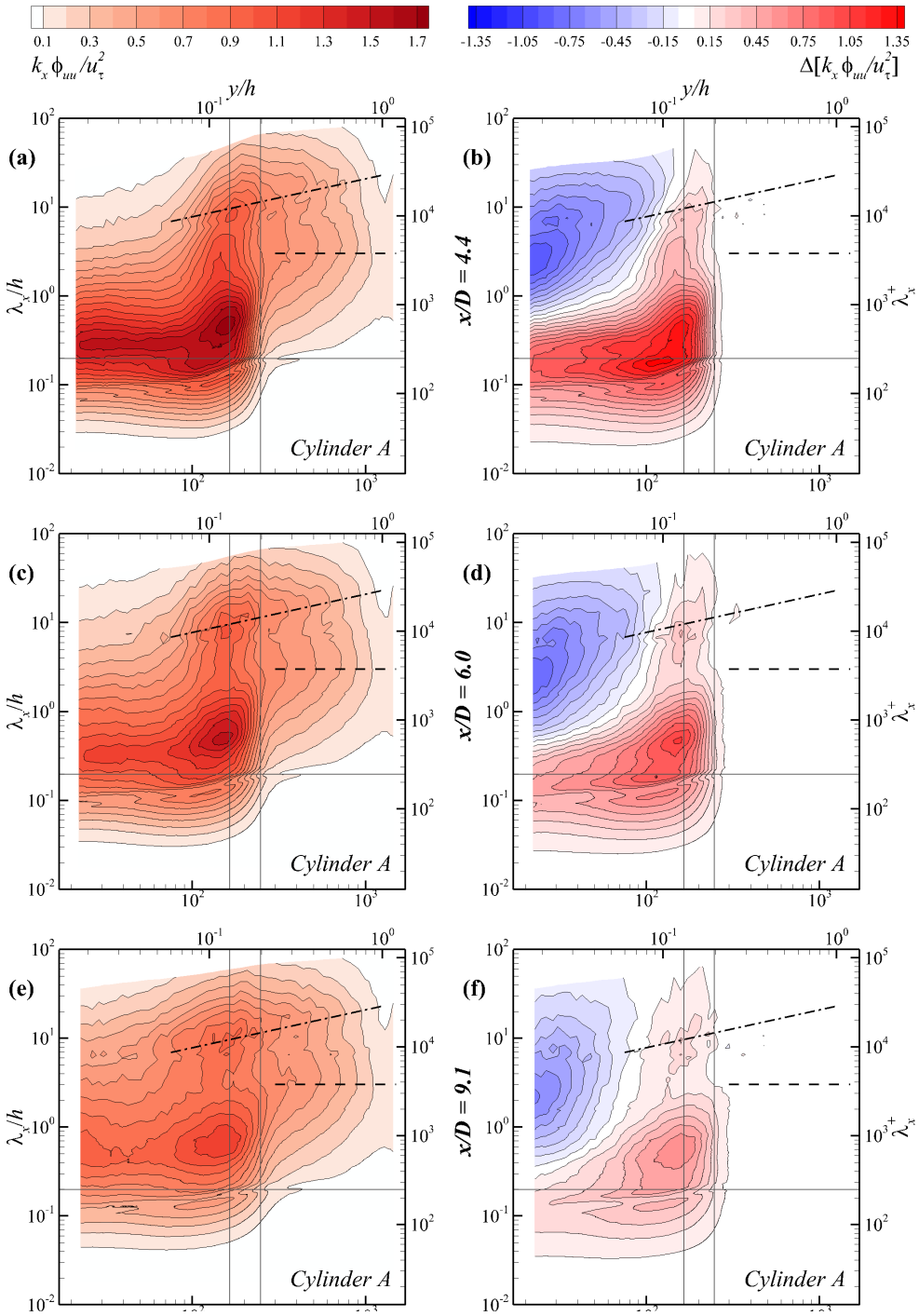

Figure 3.7: *(a,c,e)* Contours of pre-multiplied spectra ($k_x\phi_{uu}$) in the wake of Cylinder-A at the x/D locations indicated. *(b,d,f)* Contours of discrepancy spectra where positive values indicate energy addition and vice versa, relative to incident flow. The two *solid* vertical lines indicate two-thirds of cylinder height and the cylinder height, while *dash-dot* and *dashed* lines denote VLSM and LSM spectral signatures. Horizontal solid line corresponds to $\lambda_x = H$.

Figure 3.7 b in the discrepancy spectrum at $y^+ = 167$ reveals another weak peak of excess energy, which becomes evident as the perturbations dissipate with convection downstream (Figures 3.7 d and 3.7 f). This suggests a possible amplification of the existing VLSMs in the incident flow by the cylinder, or a preferential habitability to structures of such wavelength (possibly shed by the cylinder) in a turbulent channel flow environment. Thus, the observations of the perturbations by Cylinder - A to the flow can be summarized as (1) formation of a turbulent kinetic energy peak at $y/H \sim 0.64$, $\lambda/D = 5.73$ (2) alteration of the near-wall cycle where the inner peak and larger wavelength energy are suppressed, and (3) an 'amplification' of the wavelengths corresponding usually to the VLSMs in wall-bounded flows.

Subsequent decay of the discrepancy spectra contours plots with streamwise direction, in Figures 3.7 d and 3.7 f indicates a recovery of the perturbed flow towards the incident unperturbed flow. This decay clearly shows the 'enhancement' of the VLSM wavelength structures in the flow mentioned earlier, as two significant local peaks can be seen at a y location of roughly two-thirds of the cylinder height. The decay of the structures at this secondary VLSM peak appears to occur more slowly than the 'surrounding' structures (neighboring wavelengths and wall-normal positions). No VLSM-type growth of this secondary peak, as observed according to Eq. (3.1) in the unperturbed channel flow, can be seen at any streamwise position. The outer peaks formed by the cylinder decay and the inner flow closer to the wall begins to recover across all the wavelengths. This decay behavior observed in the spectra are consistent with the streamwise Reynolds normal stress recovery observed earlier in Figure 3.3.

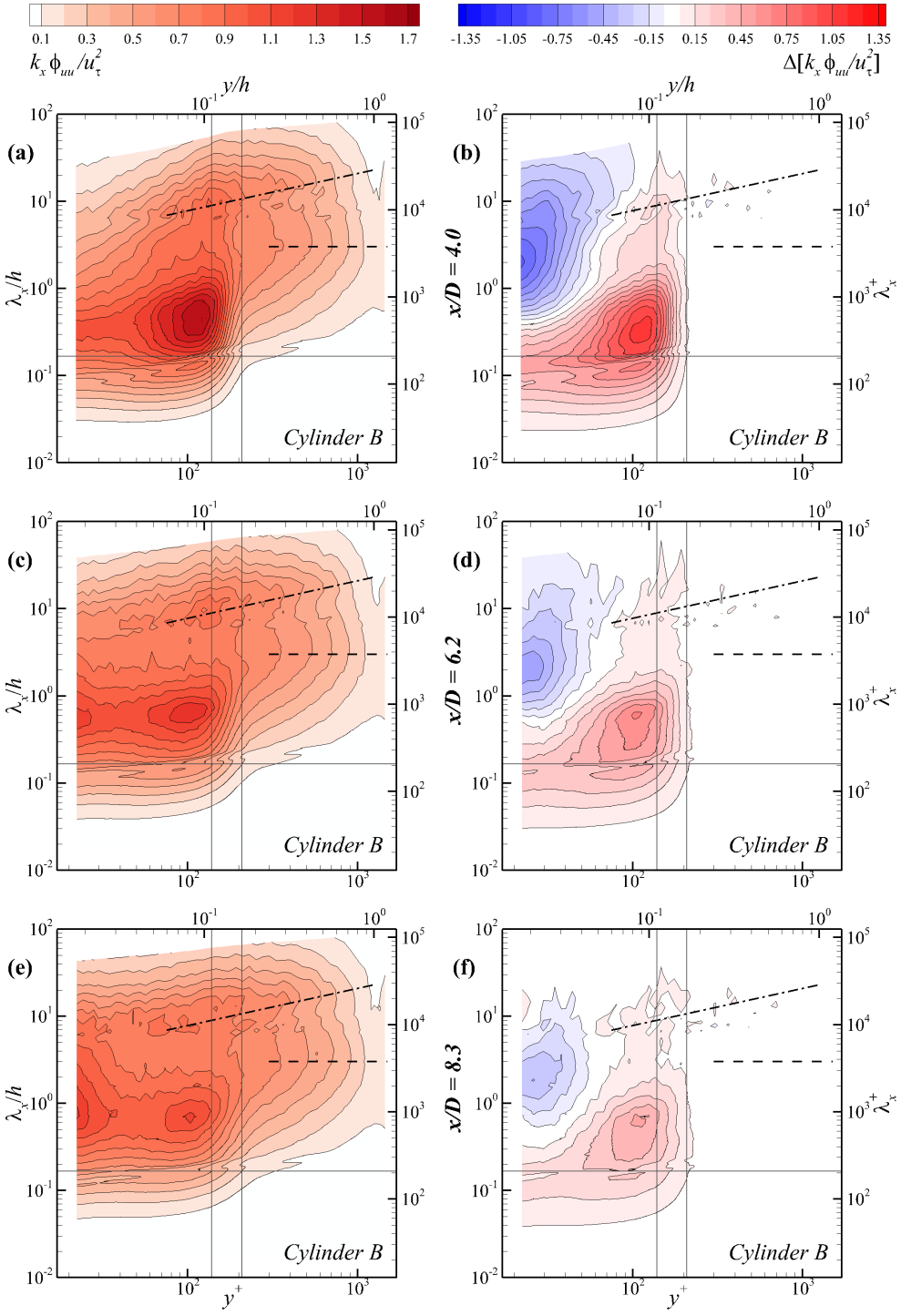

Figure 3.8: As in Figure 3.7 but for Cylinder-B ($AR = 1.76$).

Figure 3.8 shows the perturbed pre-multiplied spectra and the discrepancy spectra of the flow downstream of Cylinder - B. In the case of this lower AR cylinder, the re-emergence of the inner near-wall peak characteristic of the unperturbed channel flow (also observed in Figure 3.4) can clearly be seen with increasing downstream distance. Except for the variation of the near-wall energy distribution and recovery ($y^+ < 50$), the two cylinders appear to perturb the flow in a qualitatively similar manner. The outer maximum in the discrepancy spectrum appears to occur at $y^+ = 117$ ($y/h = 0.56$), and at wavelength $\lambda^+ = 592$ ($\lambda/h = 0.47$, $\lambda/D = 4.27$). In this regard, all the three types of perturbations observed in the composite spectra of Cylinder - A appear to be present in this Cylinder - B case as well. While both the cylinders show decaying discrepancy plots with streamwise position, meaning the flow is recovering to the unperturbed flow, there are subtle differences in the recovery between the two cylinder cases closer to the wall. There is an immediate reappearance of the near-wall peak just downstream of Cylinder - B, in contrast to that of Cylinder - A where the inner peak is only subtly seen at the farthest streamwise location ($x/D = 9.1$). From the magnitudes of the discrepancy energy levels, the recovery in the Cylinder - B appears to be faster than that of Cylinder - A. Besides these differences closer to the wall, possibly from the occurrence of different wake structures, the perturbations by both the cylinders to the incident channel flow appear qualitatively similar.

Thus, the structural modifications of the flow imposed by the wall-mounted circular cylinders are clearly evident in the pre-multiplied and discrepancy contour plots. An outer peak, owing to the cylinder, increases the turbulent kinetic energy away from the wall. The near-wall turbulent kinetic energy distribution across scales is drastically different, possibly either by

severe alteration of the existing flow, or by substitution of the near-wall turbulent structure by the cylinder wake structure. Further experimentation and analysis is needed to investigate these effects. Finally, an enhancement of the structures corresponding to the VLSM wavelengths is observed with both the cylinders. The modifications of these structures are found to decay slower than the surrounding disturbances induced by the cylinder as the flow convects downstream. This behavior suggests either an amplification of the incident VLSM structures, or a preferential habitability to the structures of such wavelengths shed by the cylinder. Further investigation needs to be carried out to explain this behavior.

3.3 Inner-Outer Interaction and Amplitude Modulation of Near Wall Scales

Recent studies have revealed strong influences of the log-layer, larger-scale motions (LSMs and VLSMs) on the near-wall flow behavior (principally the smaller-scale motions) in turbulent wall-bounded flows (Mathis et al., 2009a,b; Hutchins and Marusic, 2007). While an inner peak in $\overline{u'^2}$ from meandering structures close to the wall has been traditionally observed at $y^+ = 15$ due to structure of size $\lambda^+ \sim 1000$ (Kline et al., 1967), an outer peak within the log layer was recently observed in high Reynolds number flows at $y/\delta = 0.06$ corresponding to $\lambda \sim 6\delta$ (Hutchins and Marusic, 2007). Observations on the influence of the Reynolds number on the near-wall peak, which ought to have been independent if the latter were 'universal' to all flows, suggests a possible influence of these outer structures on the near wall cycle. More recent studies of Mathis et al. (2009a,b); Marusic et al. (2010)

have investigated and modeled this influence as amplitude modulation of the smaller-scale, near-wall motions by the larger-scale motions in the logarithmic layer that are responsible for this outer peak in $\overline{u'^2}$. By measuring and computing the correlation between the large-scale fluctuations in the log layer, and the amplitude changes of the smaller scales (via the Hilbert transform), the said influence of the former on the latter was estimated. Thus, in principle, two hot-wire simultaneous time series measurements–one in the log layer and the other closer to the wall–are needed to investigate this phenomenon. This procedure is termed '*two-point analysis*'. However, experimental evidence (Hutchins and Marusic, 2007; Mathis et al., 2009a) shows that the large-scale ($\lambda > \delta$) fluctuations in the log layer at the outer peak strongly correlate with the large-scale streamwise fluctuations close to the wall. Thus, the latter can be approximated to be a 'satisfactory' representation of the former, and this assumption enables one to do this analysis with only one hot-wire measurement close to the wall. This method is hence called '*single-point*' analysis.

The methodology for experimental analysis of the 'inner–outer interactions' between the log-layer streamwise velocity fluctuations ('outer') and the near-wall streamwise velocity fluctuations ('inner') using a single hot wire can be summarized as follows:

1. Measure the streamwise fluctuations near the wall of the turbulent flow.

2. Use Taylor's Hypothesis to convert time series into convecting spatially-stationary fluctuations (frozen field).

3. Filter the signal into fluctuations of large scales (u_L^+, with $\lambda > \lambda_c$) and

small scales ($u_s^+, \lambda_x < \lambda_c$), with a cut-off wavelength, λ_c. A spectral filter was used for the current analysis for the same purpose. The precise cutoff wavelength, λ_c, does not seem to have a significant influence, and only its relative magnitude with respect to the outer flow length scale seems significant. A range of cutoff wavelengths ranging from $0.5h$ to $2h$ was tested, and $\lambda_c = h$ seemed to be appropriate as suggested by Mathis et al. (2009a). Figure 3.9 shows a sample time series measurement close to the wall, along with the filtered large and small scales. The cut-off filter was applied at $\lambda_c = h$, and the small and large scales smaller and larger than λ_c separated and plotted for comparison. The larger (i.e., slower fluctuations) and smaller scales (i.e., faster fluctuations) can clearly be seen separated from the original fluctuating signal, and their superposition would give back the original time series.

4. Compute the Hilbert transform ($\mathbb{H}[u_s^+(t)]$) of the small scales, given by

$$\mathbb{H}(t) = \mathbb{H}[u_s^+(t)] = \frac{1}{\pi} \int_{-\infty}^{+\infty} \frac{x(\tau)}{t-\tau} \mathrm{d}\tau, \tag{3.2}$$

and the envelope function ($\mathbb{E}[u_s^+(t)]$), given by

$$\mathbb{E}(t) = \mathbb{E}[u_s^+(t)] = \sqrt{\left(u_s^+(t)\right)^2 + \mathbb{H}^2(t)} \tag{3.3}$$

The Hilbert transform, for real signals, can be used to generate the 'envelope' function of the signal, showing its amplitude variations using the Eq. (3.3). More details of Hilbert transforms, and their physical interpretation for real signals, can be found in Bendat and Piersol (2000).

5. The computed envelope function would be very noisy, with smaller fluc-

tuations super-imposed over the amplitude modulation by the larger scales. Thus, following Mathis et al. (2009a), the envelope signal can further be filtered to isolate only the larger fluctuations ($\mathbb{E}_L[u_s^+(t)]$), and the filter of same cut-off wavelength ($\lambda_c = h$) is applied in the current study. Figure 3.10 shows the small-scale fluctuations (also shown in Figure 3.9), and the envelope signal computed from Eq. (3.3), that reveals the amplitude fluctuations of the small scales ($\mathbb{E}[u_s^+(t)]$). These amplitude fluctuations are further filtered for large scales, $\mathbb{E}_L[u_s^+]$, the mean is subtracted, and in Figure 3.10, superimposed over the large-scale fluctuations of the time series signal for comparison. The correlation between the two signals can be observed clearly, with positive values of the envelope function of small scales aligning with the positive values of the large scales, and vice versa.

6. Compute the correlation coefficient (R) between the large scales (u_L^+) and the mean-subtracted, large-scale envelope of the small scales ($\mathbb{E}_L[u_s^+]$), as

$$R = \frac{\overline{u_L^+ \, \mathbb{E}_L(u_s^+)}}{\sqrt{\overline{u_L^{+2}}} \sqrt{\overline{(\mathbb{E}_L(u_s^+))^2}}}. \tag{3.4}$$

This correlation represents a measure of the inner–outer interactions– that is, influence of the large scales close to the wall (and the large scales in the log layer), on the small scales close to the wall.

This amplitude modulation (AM) analysis can be repeated for measurements at various wall normal positions to evaluate the variation of the inner–outer interactions with wall-normal position. More details of the above mentioned algorithm can be found in Mathis et al. (2009a).

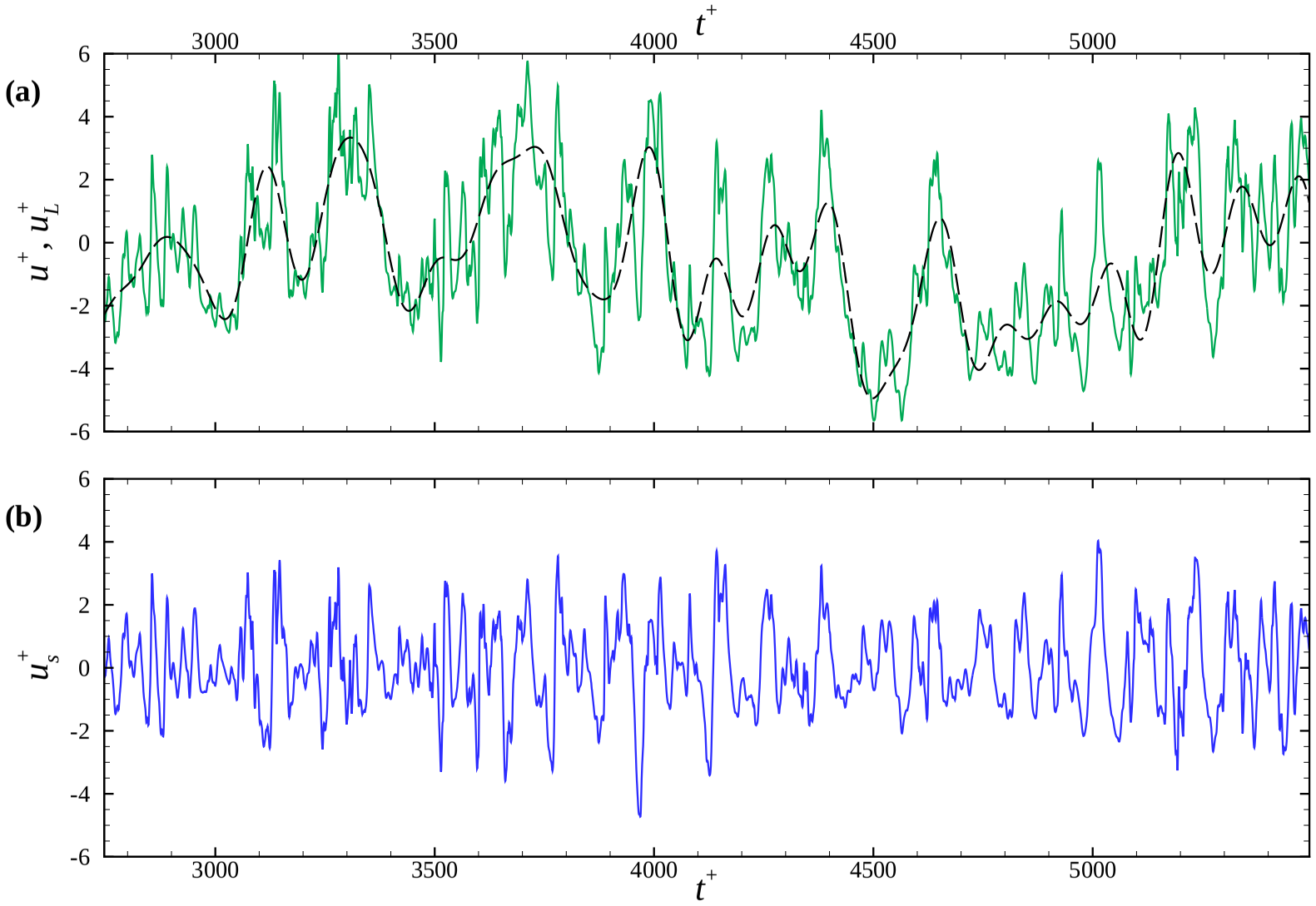

Figure 3.9: Demonstration of the spectral filter used to separate small ($u_s^+, \lambda_x < h$) and large ($u_L^+, \lambda_x > h$, *dashed line*) scales.

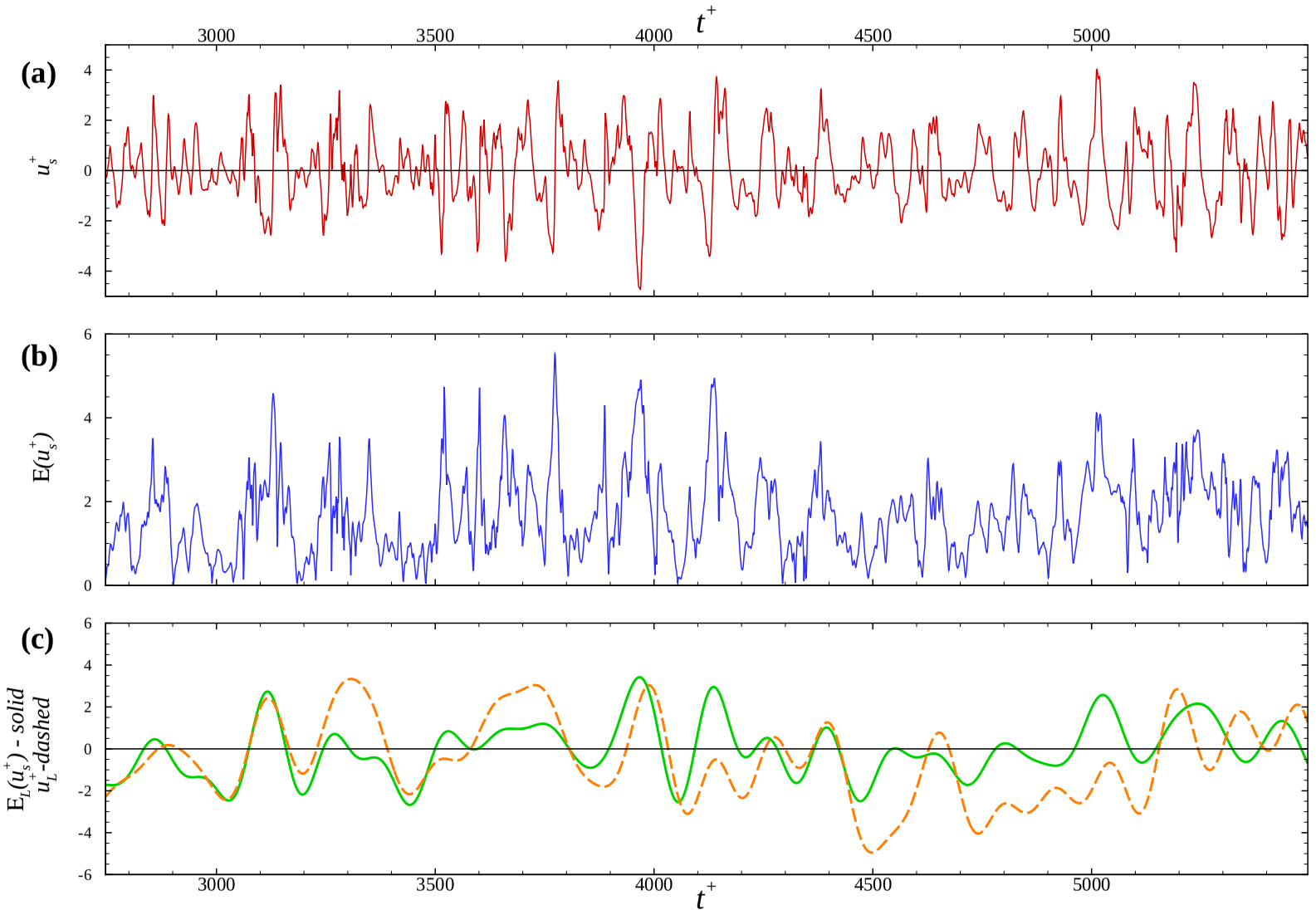

Figure 3.10: *(a)* shows the small scale fluctuations filtered in Figure 3.9, u_s^+; *(b)* shows the envelope function of u_s^+, computed using the Eq. (3.3); *(c)* shows the large scales in the envelope function, $\mathbb{E}_L[u_s^+]$, *solid*, magnified 2X for clarity. Also super imposed in *(c), dashed* is the corresponding large scale fluctuations, u_L^+, filtered and shown in Figure 3.9

Unperturbed Channel Flow

The above-summarized AM analysis was performed on all the unperturbed and perturbed channel flow measurements detailed in Table 2.3. Figures 3.11 and 3.12 show the variation of AM correlation coefficient at various wall-normal positions for Re_τ of 950 and 1250, respectively, from all the experiments. It must be noted that, while there is attenuation in the measurements of small scales due to the spatial resolution issues of the hot wire sensor, it is compensated for, to a limited extent, by the normalization by the measured fluctuating small-scale energy in Eq. (3.4) when computing the correlation coefficients. The results look quite similar to the observations made in Mathis et al. (2009b) in turbulent channel flow. In particular, the correlation coefficient starts at a peak of ~ 0.35 very close to the wall, and reduces farther away from the wall. The Reynolds number appears to change the wall-normal position at which the correlation coefficient crosses zero. As one moves farther outward from the log layer towards the channel half height, anti-correlation increases until a minimum of -0.25 at $y = 0.8h$. The anti-correlation reduces (i.e., correlation coefficient becomes less negative) just before the channel mid-height. These observations are entirely consistent with the observations made by Mathis et al. (2009b) in turbulent channel flow.

Perturbed Channel Flow

Figure 3.13 further shows the variation of the AM correlation coefficient in the flows perturbed by Cylinder - A at various streamwise locations. It can be seen that the correlation coefficient is enhanced very close to the wall, and a sudden anti-correlation appears immediately after the plateau and near two-thirds of the cylinder height, where the coefficient dips to a local minimum

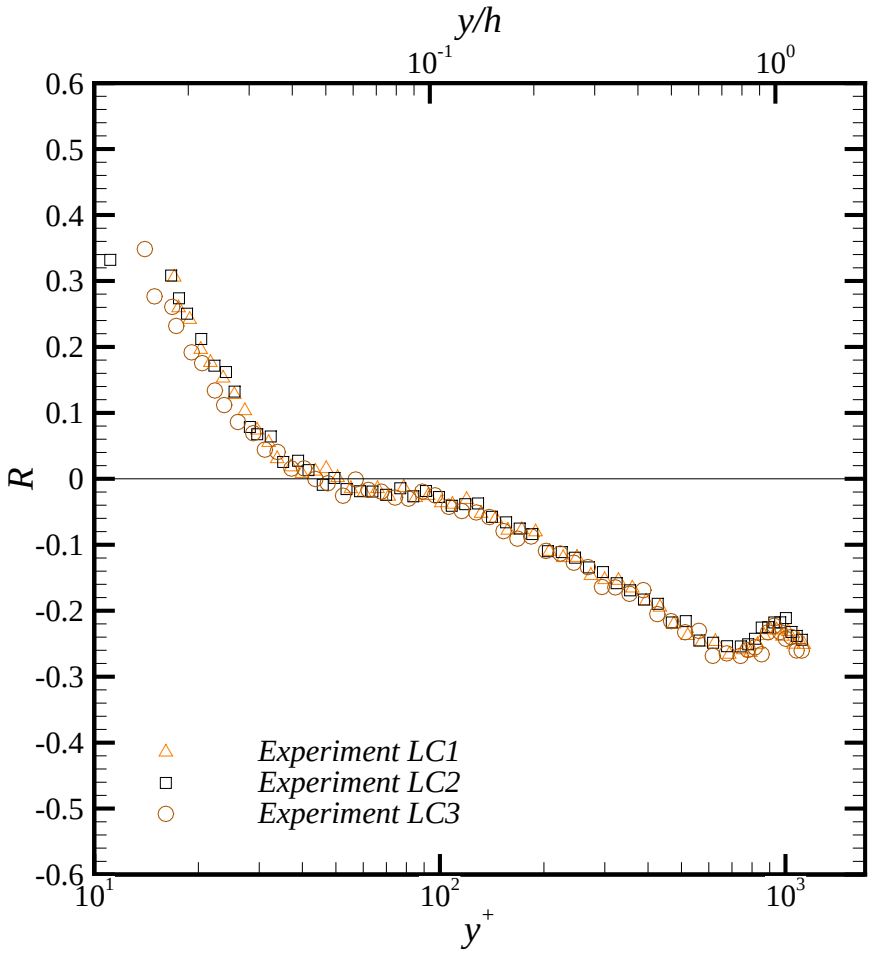

Figure 3.11: Variation of AM correlation coefficient (R) with wall-normal position for unperturbed flow at $Re_\tau = 935$.

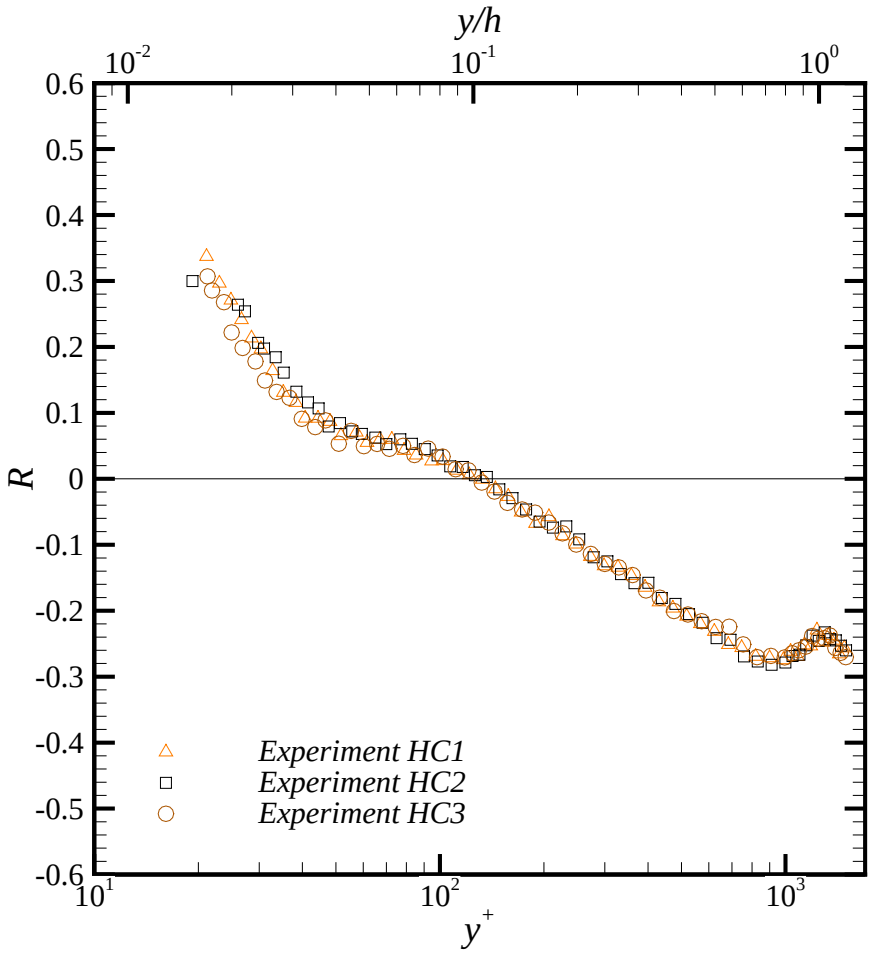

Figure 3.12: Variation of AM correlation coefficient (R) with wall-normal position for unperturbed flow at $Re_\tau = 1250$.

within the farther one-third height of the cylinder. The earlier plateau could possibly be due to the convection of the fluid farther away from the wall to regions closer, due to downwash from the cylinder tip. It is interesting to note that the zero crossing of the correlation coefficient is approximately constant, and hence the region of positive and negative correlations is similar between the incident flow and the perturbed flow trailing the cylinder. Perturbed correlation coefficient behavior by Cylinder - A recovers only slightly towards the unperturbed case at the furthest downstream measurement location.

Many similarities can be observed between the two cylinders from Figure 3.14, which shows the variation of the AM correlation coefficient with wall-normal position trailing Cylinder - B. Similar to that of Cylinder - A, a plateau of approximately constant correlation coefficient appears close to the wall, and a sharp drop to a local minimum occurs immediately after the plateau away from the wall. This local minimum seems to occur, again, within the latter one-third height of the cylinder. However, unlike Cylinder-A, a continuous recovery towards the unperturbed flow is observed with increasing downstream distance from the cylinder. Finally, a perturbation in the amplitude modulation is observed above the top of the cylinder, dissipating and propagating outwards away from the tip of the cylinder. This is unlike the other statistics observed so far in the previous sections, such as mean streamwise velocity, streamwise Reynolds normal stress and the premultiplied energy spectra.

Based upon these observations, it can be concluded that both cylinder cases perturb the flow such that the amplitude modulation is enhanced between the large scales and small scales closer to the wall. The assumption

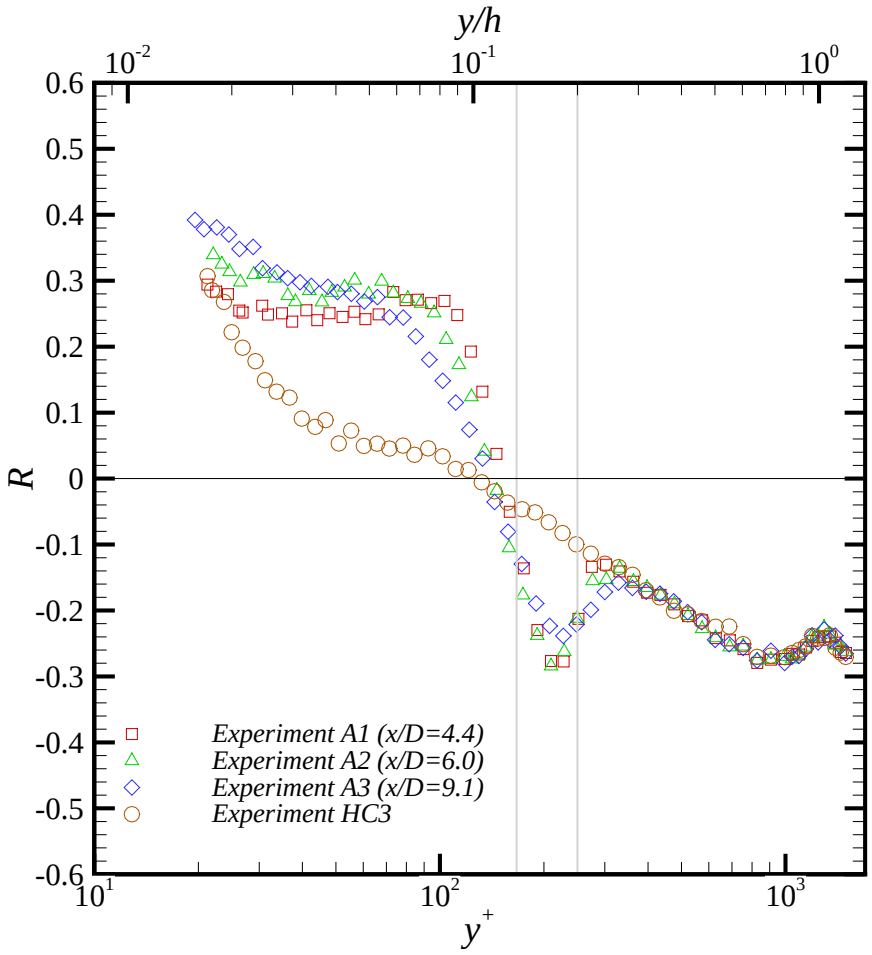

Figure 3.13: Variation of AM correlation coefficient (R) with wall-normal position for perturbed flow by Cylinder - A at various downstream positions at $Re_\tau = 1250$.

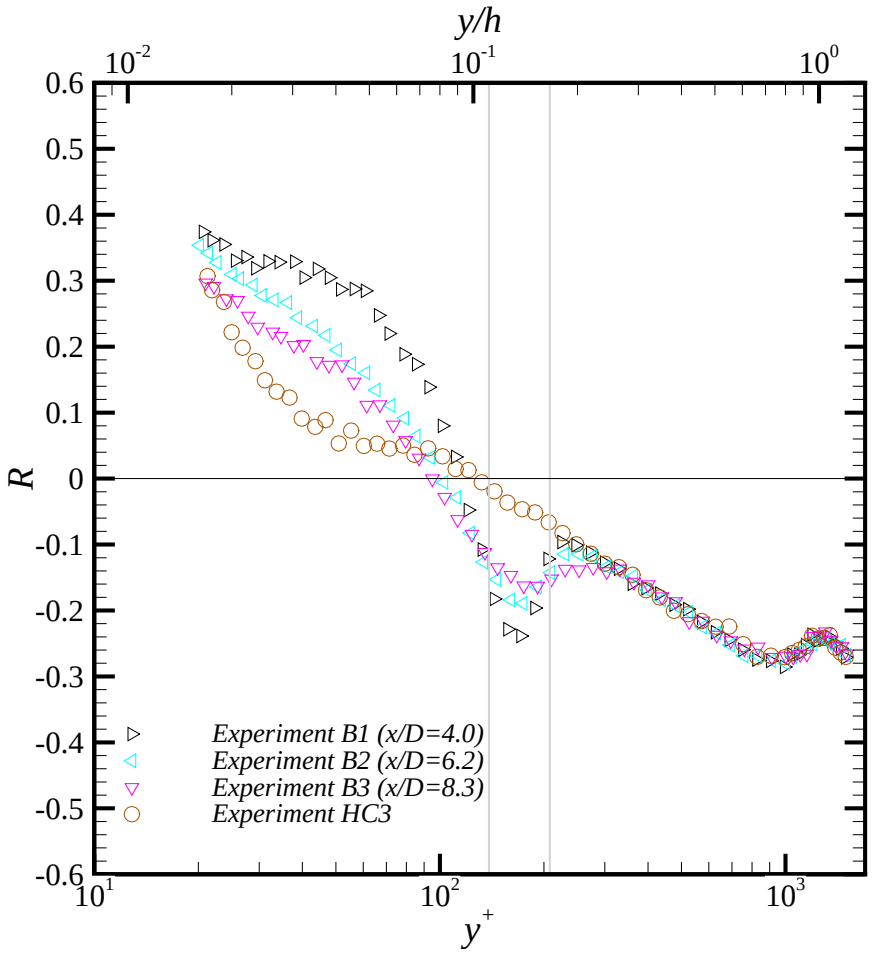

Figure 3.14: Variation of AM correlation coefficient (R) with wall-normal position for perturbed flow by Cylinder - B at various downstream positions at $Re_\tau = 1250$.

made in the 'single-point' analysis–that the large-scale motions in the log region and those near the wall are highly correlated–still must be validated for the perturbed cases. However, the increased downwash of the fluid due to the cylinder tip offers an 'intuitive' explanation for the enhanced inner-outer interaction closer to the wall. *Two-point* measurements, and multi-component measurements are required for a more detailed analysis of the flow behavior.

4 DISCUSSION AND CONCLUSIONS

The structural characteristics of turbulent channel flow was studied when perturbed with a wall-mounted cylinder using hot-wire measurements made in the wake of the cylinder. The mean and fluctuating quantities computed from the hot-wire velocity signal compared well with the observations made earlier in the literature by Ryan et al. (2011). Pre-multiplied and discrepancy spectra were computed to study the distribution of the turbulent kinetic energy as a function of scale. From this analysis, the wake of the cylinder was found to have an increased streamwise Reynolds normal stress away from the wall, and suppressed behavior closer to the wall, complementing the mean statistics observed. This additional turbulent kinetic energy peak was found to occur at a wall-normal position of two-thirds the cylinder height, and due to motions with scale $\lambda/h \sim 0.45$. The reduced near-wall streamwise turbulence kinetic energy contribution is attributed to the suppression of the large scales of the incident flow close to the wall by the presence of the cylinder, and the concomitant weakening of the canonical near-wall turbulent cycle. Further, a peak in turbulent kinetic energy, albeit smaller, is observed at wavelengths similar to the VLSM structures in the unperturbed flow. However, these perturbations to the flow ceased at wall-normal positions above the height of the cylinders based on the mean and spectral statistics analyzed in this study. Finally, the amplitude modulation effects that have satisfactorily explained the inner–outer interactions observed in

canonical wall bounded turbulent flows, have been evaluated under the unperturbed and perturbed scenarios herein. The unperturbed results closely match those reported by Mathis et al. (2009b) for turbulent channel flow. In the perturbed cases, the cylinders were found to enhance the correlation in the inner region, while a sudden correlation minima was observed away from the wall, below the tip of the cylinders. It must further be noted that the correlation maximum, occurring near the wall, was relatively unaffected. Only the fall in the correlation coefficient away from the wall was restrained.

Subsequent measurements at downstream locations indicate that the aforementioned modifications to the turbulent channel flow by the cylinders decay, and that the suppressed channel-flow characteristics from the unperturbed flow begin to redevelop. This decay has been found to be non-uniform throughout the energy spectrum. While the near-wall energy peak recovered very fast , the peak at the cylinder tip decays slower than the former. Energy at wavelengths consistent with VLSM structures was found to decay slower than the neighboring wavelengths and wall-normal positions. Finally, the AM influences were also found to decay with downstream distance, towards the unperturbed flow behavior.

Based on these observations, a few important conclusions can be drawn in concert with the pertinent literature. The perturbation of the channel flow by the cylinder is selective, and not uniform across the energy spectrum. Qualitatively similar discrepancy between the two cylinder cases, coupled with similar observations made by Jacobi and McKeon (2011b) (see Figure 16 in reference) for transverse bar perturbations in a turbulent boundary layer, suggests a preferential evolution behavior of wall bounded turbulent

flows subjected to a perturbation. Despite the fact that the perturbation of Jacobi and McKeon (2011b) is two-dimensional in nature, they have also reported the three dominant characteristics observed in the current work: (1) Suppression of the near-wall, larger-scale fluctuations, (2) formation of a perturbation energy peak in the log layer at $y/\delta \sim 0.1$ and (3) enhancement of energy at wavelengths consistent with those of the VLSM structures. Another important distinction between the work of Jacobi and McKeon (2011b) and the present effort is that the evolution of the perturbed flow in the current work is subjected to not only the turbulent outer flow, as in Jacobi and McKeon (2011b), but also to the surrounding unperturbed channel flow in the spanwise direction owing to the use of 3D perturbations herein (i.e., isolated cylinders). Thus, the present case is a fundamentally different environment for evolution of disturbances compared to Jacobi and McKeon (2011b), yet similar behavior is noted. One distinct observation was made in the current study from Jacobi and McKeon (2011b)–a positive energy discrepancy (addition of turbulent kinetic energy) was observed even at smaller wavelengths close to the wall. Such an energy addition at smaller scales was not observed in Jacobi and McKeon (2011b) who reported only energy suppression at the larger scales close to the wall owing to their 2D surface perturbation.

Finally, besides providing valuable information regarding perturbation response of a turbulent channel flow, the current work also raises a few questions that deserve additional research attention. For example, the evolution behavior of log-layer perturbations, and more importantly, the influence of the same on the evolution of the LSMs and VLSMs must be analyzed in greater depth. The influence of wall roughness on amplitude modulation behavior also deserves attention to understand the robustness and response of

the inner–outer interaction mechanisms in wall-bounded flows. The generality of this qualitatively similar (with Jacobi and McKeon (2011b)) response of the flow to perturbations needs to be evaluated over a wider class of disturbances. Doing so may provide clues that can be exploited for targeted control of wall-bounded turbulent flows.

REFERENCES

MS Adaramola, OG Akinlade, D Sumner, DJ Bergstrom, and AJ Schenstead. Turbulent wake of a finite circular cylinder of small aspect ratio. *Journal of fluids and structures*, 22(6):919–928, 2006.

RJ Adrian, CD Meinhart, and CD Tomkins. Vortex organization in the outer region of the turbulent boundary layer. *Journal of Fluid Mechanics*, 422 (1):1–54, 2000.

Ronald J Adrian. Hairpin vortex organization in wall turbulence. *Physics of Fluids*, 19:041301, 2007.

BJ Balakumar and RJ Adrian. Large-and very-large-scale motions in channel and boundary-layer flows. *Philosophical Transactions of the Royal Society A: Mathematical, Physical and Engineering Sciences*, 365(1852):665–681, 2007.

Balakumar Jothimohan Balasubramaniam. *PIV Measurements in a Solid Rocket Motor Exhaust Plume*. PhD thesis, University of Illinois at Urbana-Champaign, 2002.

Julius S Bendat and Allan G Piersol. Random data analysis and measurement procedures. *Measurement Science and Technology*, 11(12):1825, 2000.

Hans H Bruun. Hot-wire anemometry: principles and signal analysis. *Measurement Science and Technology*, 7(10), 1996.

KT Christensen and RJ Adrian. Statistical evidence of hairpin vortex packets in wall turbulence. *Journal of Fluid Mechanics*, 431:433–443, 2001.

Juan C Del Álamo and Javier Jiménez. Estimation of turbulent convection velocities and corrections to taylor's approximation. *Journal of Fluid Mechanics*, 640:5, 2009.

Juan C Del Alamo, Javier Jiménez, Paulo Zandonade, and Robert D Moser. Scaling of the energy spectra of turbulent channels. *Journal of Fluid Mechanics*, 500:135–144, 2004.

DJ Farivar. Turbulent uniform flow around cylinders of finite length. *AIAA journal*, 19(3):275–281, 1981.

Bharathram Ganapathisubramani, Ellen K Longmire, and Ivan Marusic. Characteristics of vortex packets in turbulent boundary layers. *Journal of Fluid Mechanics*, 478(35-46):35–46, 2003.

Jacob George. *Structure of 2-D and 3-D turbulent boundary layers with sparsely distributed roughness elements*. PhD thesis, Virginia Polytechnic Institute and State University, 2005.

Michele Guala, Christopher D Tomkins, Kenneth T Christensen, and Ronald J Adrian. Vortex organization in a turbulent boundary layer overlying sparse roughness elements. *Journal of Hydraulic Research*, 50(5): 465–481, 2012.

Scott E Hommema and Ronald J Adrian. Packet structure of surface eddies in the atmospheric boundary layer. *Boundary-layer meteorology*, 106(1): 147–170, 2003.

Scott Edward Hommema. *Very-large-scale motions in wall-bounded turbulent flows*. PhD thesis, University of Illinois at Urbana-Champaign, 2001.

N Hutchins, TB Nickels, I Marusic, and MS Chong. Hot-wire spatial resolution issues in wall-bounded turbulence. *Journal of Fluid Mechanics*, 635: 103, 2009.

Nicholas Hutchins and Ivan Marusic. Large-scale influences in near-wall turbulence. *Philosophical Transactions of the Royal Society A: Mathematical, Physical and Engineering Sciences*, 365(1852):647–664, 2007.

I Jacobi and BJ McKeon. Dynamic roughness perturbation of a turbulent boundary layer. *Journal of Fluid Mechanics*, 688:258, 2011a.

I Jacobi and BJ McKeon. New perspectives on the impulsive roughness-perturbation of a turbulent boundary layer. *Journal of Fluid Mechanics*, 677:179–203, 2011b.

SJ Kline, WC Reynolds, FA Schraub, and PW Runstadler. The structure of turbulent boundary layers. *Journal of Fluid Mechanics*, 30(04):741–773, 1967.

Alfred Leder. 3d-flow structures behind truncated circular cylinders. ASME, 2003.

I Marusic, R Mathis, and N Hutchins. Predictive model for wall-bounded turbulent flow. *Science*, 329(5988):193–196, 2010.

Romain Mathis, Nicholas Hutchins, and Ivan Marusic. Large-scale amplitude modulation of the small-scale structures in turbulent boundary layers. *Journal of Fluid Mechanics*, 628:311–337, 2009a.

Romain Mathis, Jason P Monty, Nicholas Hutchins, and Ivan Marusic. Comparison of large-scale amplitude modulation in turbulent boundary layers, pipes, and channel flows. *Physics of Fluids*, 21:111703, 2009b.

JP Monty, N Hutchins, HCH Ng, I Marusic, and MS Chong. A comparison of turbulent pipe, channel and boundary layer flows. *Journal of Fluid Mechanics*, 632:431, 2009.

HCH Ng, JP Monty, N Hutchins, MS Chong, and I Marusic. Comparison of turbulent channel and pipe flows with varying reynolds number. *Experiments in fluids*, 51(5):1261–1281, 2011.

Shiki Okamoto and Yukisada Sunabashiri. Vortex shedding from a circular cylinder of finite length placed on a ground plane. *Journal of fluids engineering*, 114(4):512–521, 1992.

Cecilia Ortiz-Dueñas, Mitchell D Ryan, and Ellen K Longmire. Modification of turbulent boundary layer structure using immersed wall-mounted cylinders. *Proc. Turbulence and Shear Flow Phenomena VII*, 2011.

Cheol-Woo Park and Sang-Joon Lee. Flow structure around a finite circular cylinder embedded in various atmospheric boundary layers. *Fluid Dynamics Research*, 30(4):197–215, 2002.

RJ Pattenden, SR Turnock, and X Zhang. Measurements of the flow over a low-aspect-ratio cylinder mounted on a ground plane. *Experiments in Fluids*, 39(1):10–21, 2005.

Mitchell D Ryan, Cecilia Ortiz-Dueñas, and Ellen K Longmire. Effects of simple wall-mounted cylinder arrangements on a turbulent boundary layer. *AIAA journal*, 49(10):2210–2220, 2011.

Hiroshi Sakamoto and Mikio Arie. Vortex shedding from a rectangular prism and a circular cylinder placed vertically in a turbulent boundary layer. *Journal of Fluid Mechanics*, 126:147–165, 1983.

D Sumner, JL Heseltine, and OJP Dansereau. Wake structure of a finite circular cylinder of small aspect ratio. *Experiments in Fluids*, 37(5):720–730, 2004.

Shuji Tanaka and Susumu Murata. An investigation of the wake structure and aerodynamic characteristics of a finite circular cylinder:(time-averaged wake structures behind circular cylinders with various aspect ratios). *JSME international journal. Series B, fluids and thermal engineering*, 42(2):178–187, 1999.

CD Tomkins and RJ Adrian. Spanwise structure and scale growth in turbulent boundary layers. *Journal of Fluid Mechanics*, 490(1):37–74, 2003.

Christopher David Tomkins. *The structure of turbulence over smooth and rough walls*. PhD thesis, University of Illinois at Urbana-Champaign, 2001.

HF Wang and Y Zhou. The finite-length square cylinder near wake. *Journal of Fluid Mechanics*, 638(1):453–490, 2009.

HF Wang, Yu Zhou, CK Chan, and KS Lam. Effect of initial conditions on interaction between a boundary layer and a wall-mounted finite-length-cylinder wake. *Physics of Fluids*, 18:065106, 2006.

CHK Williamson. Vortex dynamics in the cylinder wake. *Annual review of fluid mechanics*, 28(1):477–539, 1996.

Y Wu and KT Christensen. Outer-layer similarity in the presence of a practical rough-wall topography. *Physics of Fluids*, 19:085108, 2007.

Shaokai Zheng. *Perturbing spanwise modes in turbulent boundary layers*. PhD thesis, University of Minnesota, 2013.